DLR Design Challenge 2022

Dipper & AEGIS

Proposal for a remotely operated firefighting Aircraft within a System-of-Systems Mission Approach

Team	B. Berg, P. Droste, I. Kullmer-Ispas, M. Schoder, P. Trapp, F. Wolff
Academic Support	Prof. Dr. Markus Grieb
Institution	Duale Hochschule Baden-Württemberg Ravensburg
Submission Date	July 11th, 2022

Team Members

Team members from left to right:

Florian Wolff
Aerospace Engineering (Systems), 4th Semester (B. Eng.)
wolff.florian-it20@it.dhbw-ravensburg.de

Isabella Kullmer-Ispas
Aerospace Engineering (Electronics), 4th Semester (B. Eng.)
kullmer-ispas-it20@it.dhbw-ravensburg.de

Brendan Berg
Aerospace Engineering (Electronics), 4th Semester (B. Eng.)
berg.brendan-it20@it.dhbw-ravensburg.de

Pascal Trapp
Aerospace Engineering (Systems), 4th Semester (B. Eng.)
trapp.pascal-it20@it.dhbw-ravensburg.de

Paul Droste
Aerospace Engineering (Systems), 4th Semester (B. Eng.)
droste.paul-it20@it.dhbw-ravensburg.de

Magnus Schoder
Aerospace Engineering (Systems), 4th Semester (B. Eng.)
schoder.magnus-it20@it.dhbw-ravensburg.de

Declaration of Authorship

We hereby declare that the thesis submitted is our own unaided work.
All direct or indirect sources used are acknowledged as references.

We are aware that the thesis in digital form can be examined for the use of unauthorized aid and in order to determine whether the thesis as a whole or parts incorporated in it may be deemed as plagiarism.

This paper was not previously presented to another board and has not been published.

Friedrichshafen, July 11th, 2022

Brendan Berg

Paul Droste

Isabella Kullmer-Ispas

Magnus Schoder

Pascal Trapp

Florian Wolff

DHBW
Duale Hochschule
Baden-Württemberg
Ravensburg

Duale Hochschule Baden-Württemberg · Ravensburg
Fallenbrunnen 2, 88045 Friedrichshafen

Prof. Dr.-Ing. Markus Grieb
Lehrprofessor für Luft- und Raumfahrtsysteme

DHBW Ravensburg
Campus Friedrichshafen
Fallenbrunnen 2
88045 Friedrichshafen

Telefon + 49.7541.2077-452
Telefax + 49.7541.2077-198

grieb@dhbw-ravensburg.de
www.technik.dhbw-ravensburg.de

01.07.2022

Eigenständigkeitserklärung

Sehr geehrte Damen und Herren,

hiermit bestätige ich, dass die teilnehmenden Studierenden mit dem Thema:

DLR Challenge 2022

selbstständig verfasst und keine anderen als die angegebenen Quellen und Hilfsmittel benutzt haben

Friedrichshafen, den 01.07.2022

Mit freundlichen Grüßen

Prof. Dr.-Ing. Markus Grieb

DHBW Ravensburg
Campus Ravensburg
Marienplatz 2
88212 Ravensburg

Telefon + 49.751.18999-2700
Telefax + 49.751.18999-2701

DHBW Ravensburg
Campus Friedrichshafen
Fallenbrunnen 2
88045 Friedrichshafen

Telefon + 49.7541.2077-0
Telefax + 49.7541.2077-199

info@dhbw-ravensburg.de
www.dhbw-ravensburg.de

Abstract

Aerial firefighting is proven to be highly effective in mitigating the impact of wildfires on the environment. At the same time, great developments can be observed in the sector of Advanced Air Mobility, proposing sustainable and efficient More Electric Aircraft concepts.

This combination of trends and the prompt of the DLR Design Challenge 2022 motivated our team from the DHBW Ravansburg to propose the design of *Dipper* - a modular, simple and reliable yet innovative fire extinguishing aircraft. Furthermore this design is embedded in a greater systems-of-systems mission approach providing an advanced concept for optimised fleet operation, referenced as *AEGIS*. Each aircraft can carry up to 2022$[kg]$ worth of water to the site of operation while being controlled collectively in the fleet by the mission software and operating personnel. *Dipper* features a mission-specialised hybrid electric propulsion system and can scoop from bodies of water, as it is designed as an amphibious aircraft.

Zusammenfassung

Die Brandbekämpfung aus der Luft hat sich bei der Eindämmung der Auswirkungen von Waldbränden auf die Umwelt als äußerst wirksam erwiesen. Parallel werden neuartige Konzepte und Entwicklungen im Bereich der "Advanced Air Mobility" vorangetrieben, wobei vor allem nachhaltigere und effektivere Lösungen im Ansatz eines "More Electric Aircraft" angestrebt werden.

Diese Kombination von Trends und die Aufgabenstellung der DLR Design Challenge 2022 haben unser Team von der DHBW Ravansburg dazu motiviert, das Design von *Dipper* vorzuschlagen - ein modulares, simples und zuverlässiges, aber dennoch innovatives Feuerlöschflugzeug. Darüber hinaus ist dieses Design in ein größeres System-of-Systems-Missionskonzept eingebettet, das einen fortschrittlichen Ansatz für einen optimierten Flottenbetrieb bietet, welcher als *AEGIS* bezeichnet wird. Jedes Flugzeug kann bis zu 2022$[kg]$ Wasser zum Einsatzort transportieren und wird in der Flotte gemeinsam von der Einsatzsoftware und dem Bedienpersonal gesteuert. *Dipper* verfügt über ein speziell an die Mission angepasstes hybride-elektrisches Antriebssystem und kann Wasser aus Gewässern schöpfen, da es als Amphibienflugzeug konzipiert ist.

Contents

1 Introduction **1**

2 Mission-Focused Design **1**

3 Aircraft Configuration Overview **2**
3.1 Aircraft Requirements . . . 2
3.2 Consideration of Advanced Air Mobility . . . 3
3.2.1 Wildfire Suppression Discussion . . . 3
3.3 System Overview and Initial Sizing . . . 4
3.4 Mass Breakdown . . . 5

4 Technical Subsystems **6**
4.1 Aerodynamics . . . 6
4.1.1 Wing Sizing . . . 7
4.1.2 Stabilizer Sizing . . . 7
4.1.3 High-Lift Devices . . . 8
4.1.4 Stability . . . 8
4.2 Propulsion . . . 9
4.2.1 Propulsion Design Study . . . 9
4.2.2 Distributed Electric Propulsion . . . 9
4.2.3 High Lift Propellers . . . 10
4.2.4 Contra-Rotating Propellers . . . 10
4.2.5 Virtual Pitch Adjustment . . . 10
4.2.6 Propeller Performance . . . 11
4.2.7 Powertrain Configuration . . . 11
4.3 Fuselage . . . 11
4.3.1 Naval Design . . . 12
4.3.2 Airframe . . . 14
4.3.3 Landing Gear . . . 15
4.4 Fire Extinguishing System . . . 15
4.4.1 Scooping Mechanism . . . 15
4.4.2 Water Tank . . . 16
4.4.3 Water Release Mechanism . . . 16
4.4.4 Extinguishing Chemicals . . . 16
4.5 TRL Analysis . . . 17

5 Aircraft Performance **17**
5.1 Flight Characteristics . . . 17
5.1.1 Center of Gravity and Aerodynamic Center . . . 17
5.1.2 Lift- and Drag-Characteristics . . . 17
5.1.3 Payload-Range Diagram and Load Factor Diagram . . . 18
5.1.4 Service Ceiling . . . 18
5.2 Flight Profile . . . 19
5.3 Noise Reduction . . . 22

6 Mode of Application **22**
6.1 AEGIS . . . 22
6.1.1 System-of-System Approach . . . 22

6.1.2 Fleet . . . 23
6.1.3 Remote Piloting . . . 23
6.2 Operational Concept . . . 24
6.2.1 Fire Control Strategy . . . 24
6.2.2 Coastal and Inland Mission . . . 24
6.2.3 Adverse Visibility . . . 24
6.3 Alternative Use Case . . . 25
6.4 Expense Analysis . . . 25

7 Conclusion **25**

References **XII**

A Initial Sizing **XVII**

B Propulsion **XVIII**
B.1 Diagrams . . . XVIII
B.2 Propeller Calculations . . . XIX

C Aerodynamics **XX**

D Naval Design **XXI**
D.1 Beam Calculation . . . XXI
D.2 Reference Amphibious Aircraft . . . XXI
D.3 Hull and Tipfloat geometry . . . XXI
D.4 Interpolation Formula for the resistance coefficient . . . XXII
D.5 Submerged Volume and Wetted Area . . . XXII
D.6 Friction after Froude . . . XXII

E Flight Profile **XXIII**
E.1 Calculation Power Consumption . . . XXIII
E.2 Distance Calculation . . . XXIII
E.3 Takeoff Paths . . . XXIV
E.4 Scooping Profile . . . XXIV
E.5 Optimization of climb and descent angle . . . XXV

F Mode of Application **XXVII**

List of Figures

2.1 Discrete time simulation results for single aircraft . . . 2
2.2 Optimal fuel-water weight distribution for different scenarios . . . 2
2.3 Optimal cruise speed between fire and reservoir for different scenarios . . . 2
2.4 Fleet size and base capacity simulation for the example scenario . . . 2
3.1 3-Sided View of *Dipper* . . . 4
3.2 Powertrain and actuator system overview . . . 4
3.3 Initial Sizing Boundaries and permissible set of combinations . . . 5
4.1 Lift distribution of the wing . . . 7
4.2 Contra-Rotating Propeller Configuration . . . 10
4.3 Propeller Performance . . . 12
4.4 Estimation of the hull geometry based on the length-beam ratio and beam loading . . . 13
4.5 Trim angle and resistance coefficient over velocity . . . 14
4.6 Total water drag over velocity . . . 14
4.7 Schematic representation of the scooping mechanism . . . 15
4.8 water release mechanism . . . 15
4.9 model of the water tank . . . 16
4.10 water tank seals . . . 16
5.1 CG positions for different configurations . . . 18
5.2 Lift-Drag Polar . . . 19
5.3 Lift-to-Drag ratio in regard to lift coefficient . . . 19
5.4 Lift coefficient in regard to angle of attack . . . 19
5.5 Skin drag coefficient in regard to angle of attack . . . 19
5.6 Payload-Range Diagram . . . 20
5.7 Load Factor Diagram . . . 20
5.8 Rate of climb as a function of air density . . . 20
5.9 Flight Profile for the given example mission . . . 21
6.1 Proposed AEGIS operation structure . . . 23
6.2 Screenshot of the proposed *AEGIS* mission control software . . . 23
A.1 Initial Mass Estimation . . . XVII
B.1 HLP Torque curve [35] . . . XVIII
B.2 Efficiency over velocity for maximum design RPM . . . XVIII
B.3 Efficiency over advance ratio $J = \frac{v}{n \cdot D}$ . . . XVIII
B.4 Power coefficient 4 over advance ratio $J = \frac{v}{n \cdot D}$ . . . XVIII
B.5 Velocity vectors with equal RPM for front- and rear propeller . . . XIX
B.6 Velocity vectors with different RPM for front- and rear propeller . . . XIX
D.1 Dipper in Comparison to different reference Amphibious Aircraft . . . XXI
D.2 Submerged Volume and Wetted Area over velocity . . . XXII
E.1 T/O path from dry runway . . . XXIV
E.2 T/O path from water . . . XXIV
E.3 Profile scooping . . . XXIV
E.4 T/O energy consumption over γ . . . XXV
E.5 T/O distance over γ . . . XXV
E.6 base $\leftrightarrow$ water reservoir energy consumption over γ . . . XXV
E.7 base $\leftrightarrow$ water reservoir time to travel over γ . . . XXV
E.8 base $\leftrightarrow$ fire energy consumption over γ . . . XXVI
E.9 base $\leftrightarrow$ fire time to travel over γ . . . XXVI
E.10 water reservoir $\leftrightarrow$ fire energy consumption over γ . . . XXVI

E.11 water reservoir $\leftrightarrow$ fire time to travel over γ XXVI
F.1 Screenshot of the proposed *AEGIS* mission control software XXVII

List of Tables

2.1 Additional wildfire scenarios for design verification 1
3.1 Numeric Requirements 3
3.2 desired aircraft performance 5
3.3 Mass breakdown in the standard firefighting scenario 6
4.1 Wing Geometric Parameters 8
4.2 Evaluation of propulsion concepts 9
4.3 Propeller Parameters 10
4.4 Technology Readiness Level Overview 17
5.1 CG positions and static margins for different configurations 18
5.2 Energy Consumption Standard Mission 20
5.3 Performance Parameters Take-Off 21
5.4 Performance Parameters cruise 22
5.5 Performance Parameters Scooping 22
C.1 Stabilizer geometry XX
D.1 Hull Geometry Values XXI

Nomenclature

AEGIS	Aerial Extinguishing Grouped Intervention System
AR	Aspect ratio
ATC	Air Traffic Control
CS	Certification Specifications
CRP	Contra Rotating Propellers
DEP	Distributed Electric Propulsion
DLR	Deutsche Luft- und Raumfahrtgesellschaft
EFFIS	European Forest Fire Information System
EASA	European Union Aviation Safety Agency
EHA	Electro-Hydraulic Actuator
EIS	Entry into Service
EUR	Euro
HLP	High Lift Propeller
ISA	International Standard Atmosphere
LEO	Low Earth Orbit
MSL	Mean Sea Level
MTOW	Maximum Takeoff Weight
NACA	National Advisory Committee for Aeronautics
NASA	National Aeronautical and Space Agency
OEM	Operational Empty Weight
STOL	Short Takeoff and Landing
TAS	True Air Speed
TRL	Technology Readiness Level
UAV	Unmanned Aerial Vehicle

Symbols

Constants		
κ	Isentropic exponent	1.4 [-]
R	General gas constant	8.314 $\left[\frac{J}{K \cdot mol}\right]$
g	Gravity acceleration	9.81$[m/s^2]$
Roman Symbols		
a	acceleration	$[m/s^2]$
$A_{wetted,static}$	Static wetted area of Hull	$[m^2]$
b	Wing span	[m]
B_{Hull}	Width of beam	[m]
c_1/c_2	Relative airflow	[m/s]
C'_a	Beam-loading coefficient	[-]
C_D	Drag coefficient	[-]
C_L	Lift coefficient	[-]
C_m	Pitching moment coefficient	[1/rad]
C_n	Yawing moment coefficient	[1/rad]
C_P	Power coefficient	[-]
C_r	Root chord	[m]
C_t	Tip chord	[m]
$\overline{C}$	Mean aerodynamic chord	[m]
E	Energy	[J]

e	Owald Factor	[-]
GM	Metacentric height	[m]
i	Angle of incidence	[deg]
J	Advance ratio	[m/s]
K_2	Standard loading	[-]
L_{Hull}	Length of hull	[m]
Ma	Mach number	[-]
n	Revolutions per second	[1/s]
P	Power	[W]
r_h*	Tail arm from wing AC to horizontal stabilizer AC	[m]
S	Wing reference area	[m^2]
T	Thrust	[N]
t	time	[s]
U_1/U_2	Rotational velocity	[m/s]
v_1/v_2	Forward velocity	[m/s]
v_{infty}	Inflow velocity	[m/s]
v_{Hull}	Hull speed	[m/s]
$v_{planing}$	Planing speed	[m/s]
v_{minsub}	Minimal submergence speed	[m/s]
v_{tip}	Propeller tip speed	[m/s]
V	Stabilizer volume coefficient	[-]
W	Weight	[kg]
Greek Symbols		
α_t	twist angle	[deg]
$\alpha_1/alpha_2$	Angle of Attack	[deg]
η	dimensionless half-span coordinate	[-]
η	efficiency	[-]
λ	wing taper ratio	[-]
ρ	Density	[kg/m^3]
φ	sweep angle	[deg]
Subscripts		
AC	aerodynamic center	
h	horizontal stabilizer	
LE	leading edge	
CG	center of gravity	
v	vertical stabilizer	
w	wing	
wf	wing fuselage combination	

1 Introduction

In the course of the general increase in abnormal weather events accelerated by climate change, forest fires are also on the rise and devastate large areas of land every year. In Europe, 340.000 hectares were burned in 2020 [1]. Especially the Mediterranean region with its dry climate is strongly affected. However, northern countries like Germany aren't protected from forest fires either, as can be seen in media reports. In fighting these fires, the air domain is a decisive factor in addition to the units on the ground. This is also where the *Dipper* firefighting aircraft and the associated *AEGIS* mission system are located. These were developed as part of the DLR Design Challenge 2022, in which an efficient, economically viable, safe, reliable and as quiet as possible fleet of aircraft was to be designed to transport and drop water to a fire scene in the European operational area.

In this design, much emphasis was placed on an effective firefighting strategy and the fleet concept as well as the aircraft designed with the subcategories of the fuselage, aerodynamics, propulsion concept and firefighting system.

2 Mission-Focused Design

Firefighting is a time-critical mission. Quick response and continuous operation must be ensured by all mission participants. From that, multiple additional requirements and/or design goals can be derived. For one, continues aerial extinguishing operation can be ensured by operating a fleet of extinguishing aircraft. Here, a temporary downtime of a single aircraft (e.g. when refueling is needed) will not stop the entire operation. Fatigue of pilots would require a large personnel and cost overhead working in shifts. This issue is mitigated by using autonomously flying and remotely operated UAVs. Wildfire scenarios are extraordinary events that pose an imminent danger to the surroundings and also other aircrafts in the vicinity [2]. Therefore, firefighting UAVs can safely operate here without disturbance to and from existing air traffic, making it an ideal test-bench to demonstrate autonomous aerial operation in the year 2030 (Section 4.5). Autonomous aircraft need advanced sensor technologies onboard to operate. With those, night-operation can be realised, enabling a 24/7 firefighting operation that prevents the fire from spreading in a multiple-hour mission time-out.

Those and more variables factor into the efficiency of a wildfire suppression. To measure those effects, a benchmark mission was given in the Design Challenge rules. The total amount of water released at the site of operation must be counted in a 24h time frame. Additionally, typical European wildfire scenarios were utilized to further validate aircraft, fleet and operation parameters as well as find bottlenecks. Those scenarios are enlisted in table 2.1.

	Altitudes [m]			Distances [km]		
Scenario	Base	Reservoir	Water	Base-Reservoir	Reservoir-Fire	Fire-Base
Portugal 2017	700	300	630	90	9	90
Turkey 2021	12	12	12	100	20	100

Table 2.1: Additional wildfire scenarios for design verification (Sources: [3], [4])

A discrete time simulation for individual aircraft and fleet behaviour was programmed in C++[1] to make design decisions and verify fleet operation. Aircraft performance, velocity, drag, changing mass, airport handling time, airport capacity and fleet behaviour were modeled. A steady cruise between base, reservoir and the fire at 910 [m] altitude was assumed for simplification. Thus, power and energy budget calculations can not solely rely on this simulation. The simulation was used to iterate over multiple parameters and optimize water released at the fire site. Various bottlenecks were found.

[1] `https://github.com/brnd-from-mars/DLRDC22_DipperAEGIS_Simulation`

Especially the distance to the base, the maximum base handling capacity and time at the base for refueling were found to be a significant overhead. Those can be mitigated by choosing operational bases in areas prone to wildfires and installing the capacity at said airports to handle multiple aircrafts at once. Furthermore, flights to the base have to be reduced by optimizing the energy consumption between fire and reservoirs.

For the final aircraft design, figure 2.1 depicts the amount of fuel and water onboard as well as necessary cruise power, showing, that for the given example mission, our aircraft achieves 11 water scoops for each base visit.

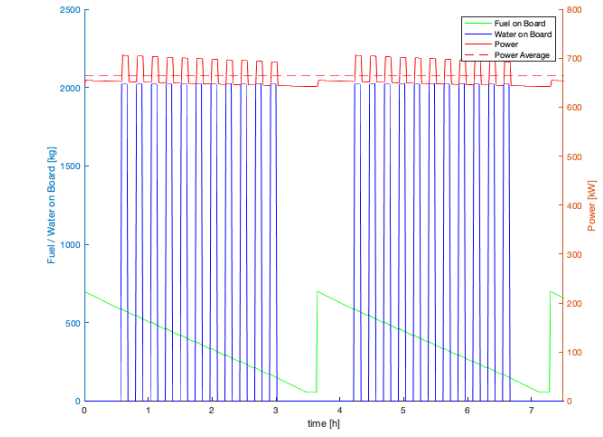

Figure 2.1: Discrete time simulation results for single aircraft

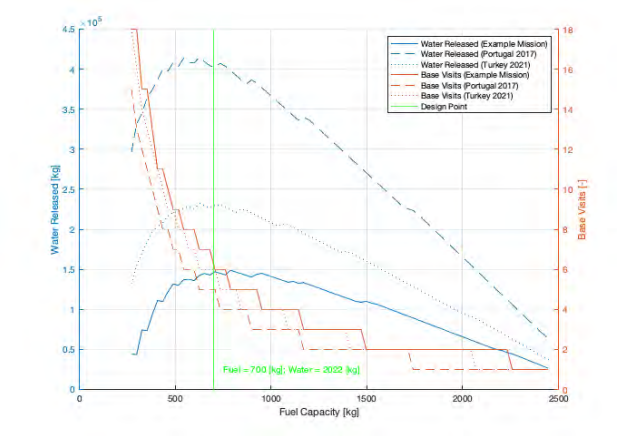

Figure 2.2: Optimal fuel-water weight distribution for different scenarios

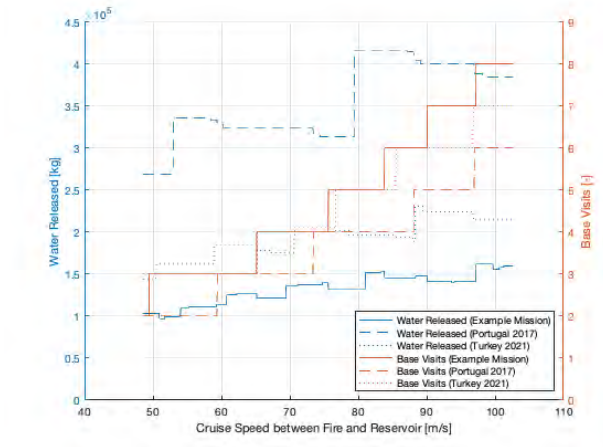

Figure 2.3: Optimal cruise speed between fire and reservoir for different scenarios

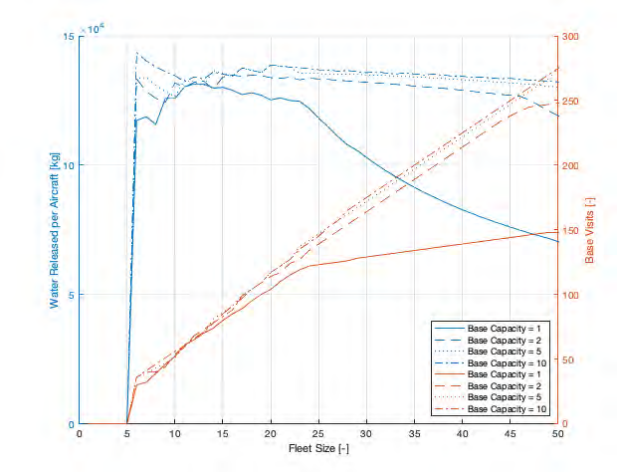

Figure 2.4: Fleet size and base capacity simulation for the example scenario

3 Aircraft Configuration Overview

3.1 Aircraft Requirements

A standard mission was specified as a benchmark. Those specification and other environmental conditions to be assumed in the design are presented below in table 3.1.

Requirement	Value
Water per firefighting attack	11 000 [l]
Maximum takeoff weight	5 670 [kg]
Mission base altitude	1 000 [ft] (MSL)
Wildfire altitude	2 000 [ft] (MSL)
Distance base to fire	75 [NM]
Distance water source to fire	15 [NM]
Atmospheric conditions	ISA Standard day + 20 [°C]
Service ceiling	8 000 [ft]
Entry into service	2030

Table 3.1: Numeric Requirements

In addition to these numerical values, there are further requirements. The goal of this design is to transport the amount of water transported within 24 hours. Other requirements include STOL capability, remote or single pilot operation, all-weather capability and noise emission considerations. Another requirement is that refueling or recharging is only possible at the base. In addition, the expected costs are to be considered, other European scenarios are to be analyzed and further considerations are to be made with regard to the operational design and other possible uses.

3.2 Consideration of Advanced Air Mobility

The further development of advanced air mobility concepts was mentioned as one approach to the development of a firefighting aircraft. Considerations in this direction are certainly valid, but a closer look reveals obstacles. For example, many of the current projects are based on battery technology, which poses problems in terms of range due to its low energy density. In the design scenario, for example, a simple distance between the base and the fire of 75 [NM] is specified. A promising urban air mobility concept such as the CityAirbus NextGen has an operational range of 80 [km] [5], i.e. approx. 43 [NM]. Thus, even if the range was doubled, not even a single mission would be possible. Another example is the Lilium Jet, which is given with a long-term range of 500 [km], about 270 [NM] [6], which would correspond to barely two missions. The X-57 of NASA as s further option is specified with a 100 [NM] range [7], which would also reach only one complete mission with a doubled range. This adds as a complicating factor that the batteries of these aircraft have to be recharged, which corresponds to considerable downtime on the ground, which in turn has a fatal effect on the amount of water carried over a longer period of time. No calculations have yet been made about the transportable payload and the required number of aircrafts, which could reveal additional obstacles. For the reasons mentioned above, it was decided against a further development of Advanced Air Mobility concepts and to focus on an independent new development.

3.2.1 Wildfire Suppression Discussion

Aerial firefighting plays a major role in forest firefighting, especially due to its ability to fight fires in remote areas with a short response time and to transport large amounts of water quickly and over long distances. A wide range of different aircraft classes are used for this purpose. These range from helicopters of all weight classes equipped with external load tanks, which take on water from natural sources, to ground-filled airtankers, which are up to the size of a converted Boeing 747. Scoopers occupy an intermediate role between these two groups. They take on water in a maneuver similar to a touch and go, in which the water is absorbed while flying on the surface of the water.

Dipper is located in the class of scoopers. This is due to the fact that it is easier to equip helicopters, cargo and passenger aircrafts in retrofits with a corresponding external load or water dropping system,

for which further development is proceeding due to general demand. However, a scooper as a seaplane has a limited operational envelope, so a separate development is more likely to be needed for this class. The necessity of scoopers is further justified by the fact that scoopers are among the most effective means of aerial firefighting [8] and therefore a core component to be preserved.

3.3 System Overview and Initial Sizing

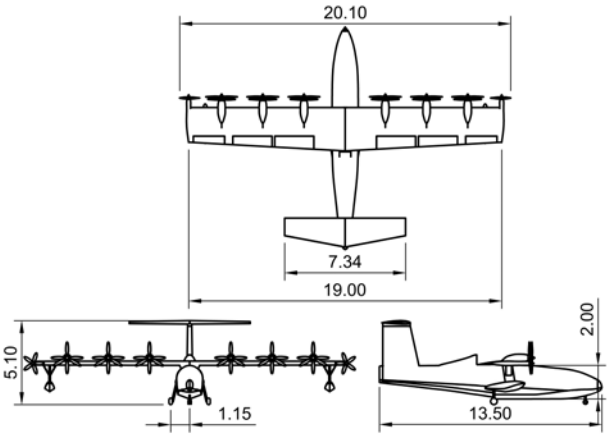

Figure 3.1: 3-Sided View of *Dipper*

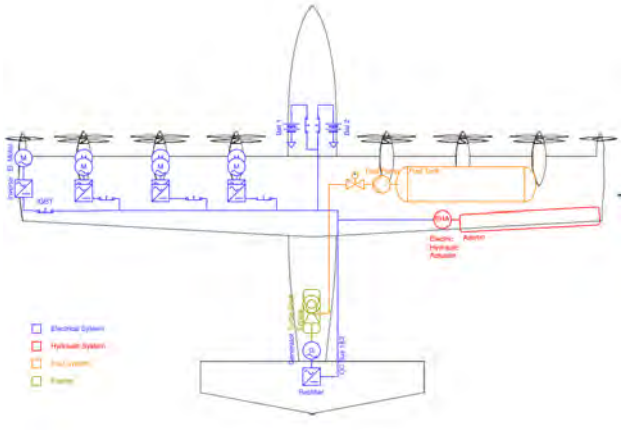

Figure 3.2: Powertrain and actuator system overview

As a main energy source, conventional jet fuel was chosen, which is converted into mechanical energy in a turboshaft engine and electrical energy with generators. Due to the early EIS in 2030, it was decided against implementation of new propulsion concepts such as hydrogen. It is assumed that hydrogen technology could first be used for short-haul flights from 2035 [9]. Furthermore, the design cannot rely solely on installed hydrogen infrastructure as it may be installed first at large commercial airports where the need is most likely to exist. Smaller airports in more sparsely populated areas could have access to a hydrogen supply only much later. However, because the general number and geographic distribution of these airports make them more suitable as an operational base for aerial firefighting to respond quickly and specifically, it must be assumed that conventional power supplies will have to be relied upon. Figure 3.2 depicts the powertrain and actuator system overview.

A *Dipper* unit is designed as an amphibious aircraft with a seaplane hull. This was chosen to allow scooping on lakes and the sea within the operational concept, which enables a fast, local and reliable supply of water for firefighting. The ability to land on runways is necessary to avoid the sole dependence on waterways and seaports, to ensure reliable fuel supply to aircrafts and accessibility for ground engineering operations, and to enable operations from inland regions. A flying boat was chosen as the hull concept due to a variety of factors. On the one hand, this design makes the seaplane more stable in rough water, and on the other hand, the ratio of payload to total weight is better. The disadvantage of this concept is said to be the unconventional control system, since the aircraft behaves differently in certain conditions than its land-based counterpart. However, this is not a disadvantageous factor in this project, as the control is computer-aided and thus the influence of the human factor is reduced. [10]

As a starting point in the design process, the method of determining wing loading and power loading as proposed by Sadraey [11] was used. By this method, the two parameters are treated as the only variables for different mission aspects of the aircraft to be designed. In combination with some general assumptions about more specific aircraft parameters such as the maximum lift

coefficients, a set of boundaries can be derived. For the aircraft to fulfil all the desired characteristics the chosen combination of wing and power loading needs to lie within all boundaries. Figure 3.3 shows the boundaries resulting from the desired characteristics as shown in table 3.2 as well as the set of permissible combinations (coloured in green). In general, selecting the point with the highest possible power loading is advantageous since it minimizes the aircraft power and by extension fuel consumption. In this case however, this would result in a very low value for the wing loading. This would lead to a higher wing span, increasing the ground handling effort. As such, the values $W/P = 0.045[kg/W]$ and $W/S = 1200[N/m^2]$ were chosen to reduce wing area by increasing engine power to compensate while still keeping a comfortable margin to the stall speed boundary dictated by CS-23 [12]. This approach also increases maneuverability due to decreased wing bending moments. Combining the chosen design point with the MTOW, the initial absolute power and wing area estimates of the aircraft equal $P = 1256[kW]$ and $S = 47[m^2]$. These values were modified later in the design process, resulting in the values given in section 4.2 and section 4.1.1.

Requirement	Desired value	Reasoning
Stall Speed	$33[m/s]$	at sea level ($\rho = 1.225[kg/m^3]$) [12]
maximum airspeed	105 [m/s]	comparison with other fire suppression aircraft
rate of climb	$12[m/s]$	comparison with other fire suppression aircraft
take-off run	$450[m/s]$	on soft, unpaved ground (friction coefficient 0.2 [11])
service ceiling	$8500[ft] \approx 2600[m]$	rate of climb of $100[fps]$ achievable

Table 3.2: desired aircraft performance

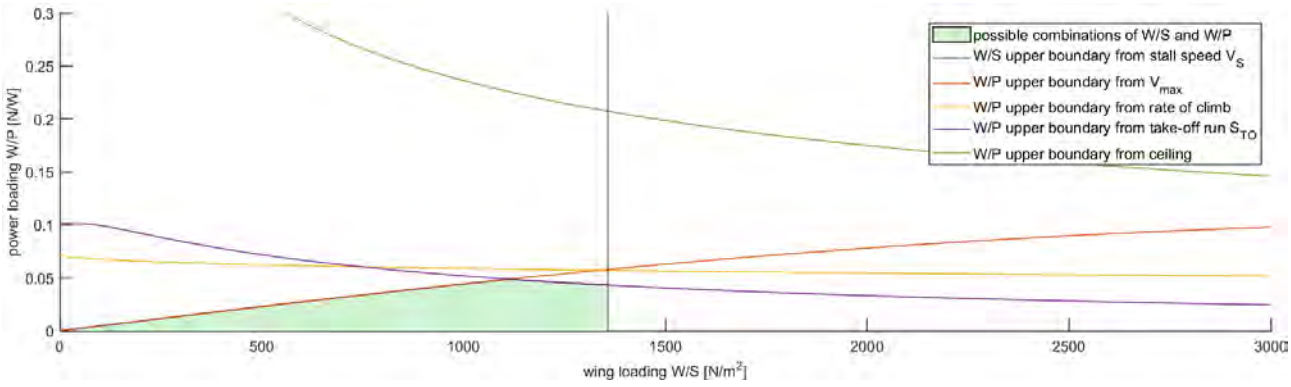

Figure 3.3: Initial Sizing Boundaries and permissible set of combinations

3.4 Mass Breakdown

An initial starting point for the mass estimation was made by comparing *Dipper* to other amphibious [13] and firefighting [14] aircrafts. A design ratio between OEW and MTOW of 52 % was initially chosen. This ratio coincides with the rapid sizing method [15] considering weight saving due to technological advancements since 1986 [16]. This value was adjusted to 47.7 % after an iterative design process and estimation of major subsystems with the methods according to Nicolai and Raymer in Gudmundsson [17].

The remaining mass will be distributed to payload and fuel. For this, the optimal water-to-fuel ratio was determined for multiple scenarios using the simulation in section 2. A fuel weight off 700 [kg] and a water capacity of 2022 [kg] was found to yield the best water output for a single aircraft at the fire site (Figure 2.2).

	Mass [kg]	Reasoning and Source
Fuselage	463	Fuselage Weight acc. to Nicolai
Wing	674	Wing Weight acc. to Raymer
Vertical Tail	24	Vertical Tail Weight acc. to Raymer
Horizontal Tail	38	Horizontal Tail Weight acc. to Raymer
Landing Gear	162	Landing Gear Weight acc. to Raymer
Structural Weight	1361	
Fuel System	54	Fuel System Weight acc. to Raymer
Turboshaft-Engine	300	$4300[W/kg]$; Engine Weight acc. to Raymer
Electric Motors	227	Ref. Motor EMR20 [18] incl. external cooling system
Battery	250	$3[kW/kg]$, see chapter 4.2.7
Generator	136	Similar to Electric Motor
Power Cables	55	$2.5[kV]$-System, two redundant power busses [19]
Flight Control System	150	Flight Control System acc. to Raymer
Remaining Subsystems	175	Sensors, Communication, ...
Operational Empty Weight	2708	
Retardant	240	Section 4.4.4
Water	2022	Simulation (Figure 2.2)
Fuel	700	Simulation (Figure 2.2)
Maximum Takeoff Weight	5670	

Table 3.3: Mass breakdown in the standard firefighting scenario. For maximal range, up to 1500 [kg] of fuel and 1462 [kg] of payload can be used.

4 Technical Subsystems

4.1 Aerodynamics

Amphibious aircraft have a unique position in the world of aeroplanes as they need to be able to maneuver both on water and land. This places some very important constraints on the design of the aerodynamics. Most importantly, take-off from water generates a water spray and bow wave due to water being displaced by the motion of the aircraft hull. Naturally, this presents a danger to any propulsive components such as propeller or jet intake blades hitting the water droplets generated. Furthermore, the aerodynamic performance of a wing covered by a water film decreases dramatically [20, 21]. This lead to the requirement for the wing and stabilizer position to be moved outside of the water spray zone. Therefore, a high-wing configuration is chosen as it provides the desired protection of both wing and propellers. More specifically, the lifting surface is designed as a shoulder-wing to increase the strength of the wing spar by keeping it as one continuous part, decreasing stress concentration by eliminating joints needed for both wing halves.

The stabilizer needs to be placed outside of the water spray zone, as well. For this purpose, the Canadair CL-415 employs a cruci-form tail configuration. While this increases structural integrity of the tail and increases space for flight control actuators by being attached at the thicker part of the vertical stabilizer it also contains a certain risk. Namely, the lower position of the horizontal stabilizer may result in it lying in the wake of the main wing at higher angles of attack. This drastically decreases tail efficiency which can cause the pilot to lose their ability to control the pitch, a phenomenon referred to as "deep stall" [22]. It is therefore necessary to position the horizontal stabilizer either above or below the suspected wing wake region. Since a low position is not possible due to water spray concerns, a high tail position is selected, more specifically a T-tail configuration. This configuration still has a risk of deep stall but it may be reduced down to an acceptable level by careful design. A V-tail might

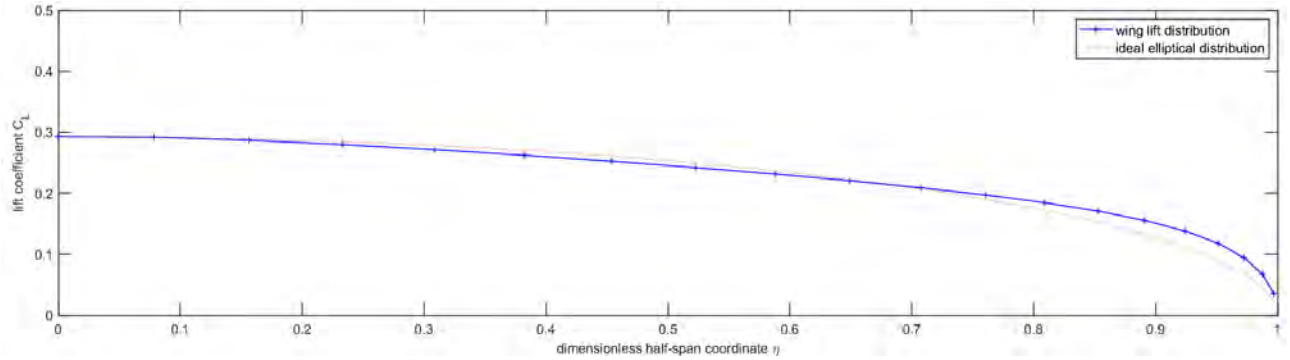

Figure 4.1: Lift distribution of the wing

also be chosen but causes additional complexity due to its coupled control surfaces and is therefore discarded.

It should also be mentioned here that due to the propulsion concept and its energy supply, electric hydraulic actuators are used to control the control surfaces and high-lift devices. [23]

4.1.1 Wing Sizing

As explained in section 3.3 the initial wing loading was chosen as $(W/S)_{init} = 1200[N/m^2]$. As the next step in the wing design, a representative airfoil was chosen. Due to the low desired maximum airspeed and the need for a low stall speed to achieve short take-off distances, an airfoil optimized for low Reynolds numbers was needed. A very high camber is undesirable as it increases the zero angle of attack lift coefficient and therefore the wing wake size [11], increasing risk of deep stall. The Selig-3002 [24] airfoil provides a good compromise between lift at low Reynolds numbers, manageable camber and adequate cross-sectional area for fuel tanks. Additionally, the airfoil provides gentle stall characteristics which improves recoverability of unstable flight states during missions.

The wing aspect ratio $AR = \frac{b^2}{S}$ determines both aerodynamic efficiency and structural stresses. A higher AR leads to higher aerodynamic efficiency but also higher bending moments and therefore higher structural weight. For transport aircraft, an aspect ratio of $AR \approx 8$ is often chosen as a compromise. Due to the influence of terrain on aerial firefighting missions, risky maneuvers are sometimes needed. To ensure the safety of the aircraft, it is imperative for the wing root to stall before the wing tip to preserve aileron control authority. As such, in addition to its other favourable properties such as constant downwash [25], an elliptical lift distribution is desirable. Table 4.1 shows the geometric parameters chosen to achieve a nearly elliptical distribution and the resulting aerodynamic properties. Figure 4.1 shows the lift distribution for the airplane in a horizontal configuration. This lift distribution was based on averaging the fuel and water weight over the different flight phases and designing the wing to provide the lift coefficient needed for horizontal flight at this weight. Since leading edge sweep does not have an appreciable effect on drag at the chosen airspeeds, the wing is left unswept to avoid perpendicular dynamic pressure losses from sweep angle.

The longitudinal wing position from the aircraft nose to the wing leading edge was determined as $x_{LE} = 4.9[m]$ through an iterative process as described in section 5.1.1.

4.1.2 Stabilizer Sizing

As explained previously, a T-tail configuration was chosen for the horizontal stabilizer. For this, the standard method of determining the horizontal tail paramters may be applied in using the static stability requirement of $\frac{\partial C_m}{\partial \alpha} = C_{m\alpha} < 0$. Using a rough estimate for the horizontal stabilizer volume coefficient $V_h = \frac{r_h*}{\overline{C}} \frac{S_h}{S} \approx 0.7$ that is based on the configuration of other transport aircraft, the

wing span b	19	$[m]$
root chord $C_{r,w}$	2.64	$[m]$
tip chord $C_{t,w}$	2.11	$[m]$
angle of incidence i_w	0.2	$[deg]$
twist angle $\alpha_{t,w}$	-2.0	$[deg]$
leading edge sweep $\varphi_{LE,w}$	0	$[deg]$
wing area S	45.125	$[m^2]$
aspect ratio AR	8	$[-]$
mean aerodynamic chord $\overline{C}$	2.38	$[m]$
taper ratio λ	0.80	$[-]$

Table 4.1: Wing Geometric Parameters

horizontal stabilizer tail arm r_h* was calculated by searching for a minimum in wetted area (and thereby drag) resulting from the tail configuration [11]. This returned a range $r_h* = 5.74...7.31[m]$. From constraints on the aircraft center of gravity (see section 5.1.1, the value $r_h* = 6.5[m]$ was chosen. From this the horizontal stabilizer planform area was calculated. The aspect ratio was chosen to be lower than that of the wings to reduce structural stress and thereby weight.

A similar approach was chosen to design the vertical stabilizer, using $\frac{\partial C_n}{\partial \beta} = C_{n\beta} > 0$ as the directional stability requirement. The desired vertical stabilizer volume coefficient was chosen as $V_v \approx 0.04$. This tends toward the lower range of possible values to ensure that the plane has adequate controllability and maneuverability, since higher static stability decreases control performance. The aspect ratio of the vertical tail was chosen to be low, as well, to provide adequate structural support for the forces acting on both vertical and horizontal stabilizer.

Table C.1 gives an overview of the chosen values of both horizontal and vertical tail and the resulting aerodynamic parameters.

4.1.3 High-Lift Devices

To achieve both the stall speed requirement of CS-23 [12] and the required landing and take-off performance, a high-lift system is needed. To reduce complexity and therefore maintenance cost as well as error susceptibility, a simple plain flap system is used on the wing trailing edge. The flaps are split into two components on each side, to provide redundancy and better controllability. Using the lift increase estimate $\Delta C_{L,f} = 0.7$ for a plain flap provided by Sadraey [11], the maximum lift coefficient results in $C_{L,max} = 2.3$ with the maximum lift coefficient of the wing airfoil.

4.1.4 Stability

The fulfilment of static stability may be checked by using the formulations for $C_{n\beta}$ and $C_{m\alpha}$. The position of the center of gravity $\frac{x_{CG}}{\overline{C}} = 0.241$ and the aerodynamic center $\frac{x_{AC}}{\overline{C}} = 0.54$ as described in further detail in section 5.1.1 may be used to deduce that static stability is achieved. More specifically the pitching moment coefficient slope is $C_{m\alpha} = -0.837[rad^{-1}] < 0$ when estimating the downwash angle slope according to Nelson [26].

The static directional stability may be checked through the equations provided by Nelson [26]. This results in a fuselage and wing contribution to directional stability of $C_{n\beta,wf} = -0.0593[rad^{-1}]$ and a vertical stabilizer contribution of $C_{n\beta,v} = 0.123$ for a total yawing moment coefficient slope of $C_{n\beta} = 0.0640[rad^{-1}]$.

As can be gathered from these values, the aircraft is statically stable. The wing-fuselage contribution may however need to be checked in flight testing due to possibility of the uncommon geometry

of the fuselage not correlating well with the empirical estimation provided by [26]. Dynamic Stability such as Dutch Roll and spiral characteristics should be tested for as well.

4.2 Propulsion

Dipper is configured with a series hybrid propulsion System equipped with 14 forward facing propellers powered by electric motors. A turbo-shaft turbine and a battery provide electric energy. The following section explains the reasons for choosing a series hybrid system, the propeller- and engine sizing and the achieved performance.

4.2.1 Propulsion Design Study

Dipper's propulsion system has to operate effectively in lower speed to achieve its STOL capability and for a quick escape in the water-dropping-process. Thus a propeller driven system was chosen, since they fulfill this characteristics in contrast to turbofan engines.

To choose a suitable drive for the propeller an evaluation for possible concepts was made. A hydrogen powered system was excluded, since hydrogen would be particularly implemented in the aviation industry by 2030 [27]. Thus reliable and quick supply of hydrogen for small airports is improbable til 2030. An evaluation for suitable concepts was made in Table 4.2.

Parameter	**Weighting**	All-Electric	Turboprop	Series Hybrid	Parallel Hybrid
Operating cost	30%	4	3	5	3
Acquisition cost	20%	3	5	2	4
Noise	10%	5	1	4	2
Weight	30%	1	5	4	3
Environmental impact	10%	5	1	3	2

Table 4.2: Evaluation of propulsion concepts according to data by [28] [29] [30] [31] rated from 1 (worst) to 5 (best)

The choice was made for a serial drive system as it is the most advantageous for the given use case with an average of 3.8 points. It also offers the possibility to switch to a hydrogen driven power system in the future and to use distributed electric propulsion (section 4.2.2). The architecture for the serial drive train is shown in figure 3.2.

4.2.2 Distributed Electric Propulsion

The distributed electric propulsion used for *Dipper* uses multiple electric motor systems to increase the aerodynamic efficiency of the aircraft. *Dipper* has six propulsive elements attached on the upper side of the wing with two contra-rotating propellers (section 4.2.4) each. The configuration increases the dynamic pressure on the upper side of the wings and thus the lift coefficient at low speeds [32]. The corresponding configuration can be seen in figure 4.2. The motor dimensions were set with a comparable reference engine [18]. The nacelle was designed to accommodate the electric motors and an appropriate cooling system. Furthermore *Dipper* has two high lift propellers (section 4.2.3) on the wing tips to reduce the vortex drag. The vortex drag is inversely proportional to the velocity [33], thus the system increases efficiency at lower speeds.

In addition, with electric motors it is possible to recover potential energy during descent phase by using recuperation [34]. It has been shown that the use of propellers optimized for recuperation can reduce overall energy consumption by up to 19% [34].

4.2.3 High Lift Propellers

High lift propellers (HLP) were designed by NASA to operate in low speed to produce maximum thrust in the takeoff phase [35]. The design has a constant propeller torque up to stall speed and decreases linearly to minimum torque afterwards (figure B.1). In the chosen design speed of 54 [m/s], the propeller blades fold and conform with their nacelle to reduce propeller generated drag [35]. At this speed, the parasitic drag becomes higher than the vortex drag, so the parasitic drag decreases in importance. The HLPs for *Dipper* were scaled for *Dipper* by a factor of 10 and the approximation was made that the produced thrust and power is proportional to the torque of the HLPs.

4.2.4 Contra-Rotating Propellers

Contra-rotating propellers (CRP) are positioned in series in the longitudinal direction. A contra-rotating configuration cancels out resulting torque acting on the wing structure, thus lowering the wings structural mass [36]. Also, contra-rotating propellers were found to be up to more 16 percent efficient than single-rotating propellers [37] by canceling out swirl losses [36]. One big issue with CRPs is the produced noise. This can be counteracted by a different blade count for the forward and the afterward propeller so the blades pass each other at different times [36]. The chosen blade count (table 4.3) is a compromise between higher efficiency achieved by fewer blades and a higher blade count to allow the diameter to be reduced [17]. The latter increases the ground clearance and reduces the generated noise.

The front Blade Angle was chosen by plotting efficiency over velocity for different blade angles (figure B.2) such that the efficiency peak for maximum RPM is at cruise velocity. The data was acquired by digitising the wind tunnel test data by NACA [37] (figure B.2). The rear pitch has to be higher, since the flow velocity has a different direction (section 4.2.5). The ratio between both angles was estimated by comparing front and rear angles from [38]. The diameter is iterated in combination with the RPM to not exceed the propeller tip mach number Ma_{max}=0.85 (equation 5). According to Dubs [39], at this point the noise level is at a acceptable level. The diameter was validated through a estimation formula by Gudmundsson [17] and the maximum RPM was found with a reference electric motor [40].

Blade Count		Pitch Angle				
Front	Rear	Front	Rear	Blade Diameter	Maximum RPM	Maximum Tip Mach Number
4	3	25[°]	45[°]	1.8 [m]	3250	0.85

Table 4.3: Propeller Parameters

Figure 4.2: Contra-Rotating Propeller Configuration

4.2.5 Virtual Pitch Adjustment

Although the CRPs have a fixed pitch, the effective angle of attack (AoA) of the propeller blades can be varied through the RPM and the true airspeed (TAS). Since each electric motor can vary its

RPM differently, it is possible to achieve a different AoA for each propeller. Also the AoA of the rear propeller can be varied through the induced vortex velocity of the front propeller. An illustration can be seen in figure B.5 and B.6. In the figure it can be seen that the front propeller rotation speed increases, resulting in an AoA increase of the rear propeller. Since the efficiency is dependent on the propeller AoA an optimal combination of RPM for each propeller at a desired velocity can be found. This technology is enabled by the possibility of powering two propellers with two decoupled motors on the same axis.

4.2.6 Propeller Performance

The propeller thrust of the CRPs was determined using wind tunnel test data by NACA [37] for 4-bladed contra-rotating propellers. The plots for the pressure coefficient c_P and the efficiency η over the advance ratio J were digitized and interpolated in dependence of J. The thrust curve (figure 4.3) was calculated using equation 1. Using data from 1942, the estimated thrust can be treated as a conservative consumption.

$$T = \frac{P \cdot \eta(J)}{v} = \frac{2 \cdot Q \cdot \pi \cdot n \cdot \eta}{v} = \frac{\rho \cdot n^3 \cdot D^5}{v} \cdot c_P(J) \cdot \eta(J) \qquad J = \frac{v}{n \cdot D} \tag{1}$$

The thrust curve was plotted at cruise conditions by varying RPM and velocity and determining the maximum thrust value for every velocity. The aerodynamic power results from equation 2 by [17]. For validation, the electrical power was plotted using equation 3 by [17]. With a maximum torque of 408 [Nm] and maximum RPM of 3250, the results fit into the conditions for the reference electric motors [18][40].

4.2.7 Powertrain Configuration

Turboshaft engines have already achieved an acceptable level of performance, therefore an reference engine [41] has been used. The power and weight were scaled by the factor 1.08 to fit for the design conditions. The turboshaft power was set to 800 [kW] to cover the cruise power and to recharge the battery in the same time 2.1. For takeoff and climb, the engine power can be increased up to 919 [kW].

The battery size was estimated that a water takeoff and safe landing can be done with only battery power to guarantee engine-out capability. A high-power battery will be needed as frequent climbs are expected for the mission. With a power density of 3 [kW/kg] [42], the battery delivers up to 750 [kW]. This can maintain a climb rate of 10 [m/s] for about 4 minutes when the battery is fully charged. The energy density in 2030 for the given power density was predicted with source [43] and [44] to 200 [Wh/kg]. Since the energy density estimation for 2030 is chosen conservative, the assumption was made that the battery installation mass equals the battery cell mass. For redundancy purposes the battery system is divided in two separate units.

4.3 Fuselage

Compared to an ordinary aircraft fuselage which is designed to be lightweight, aerodynamic and high-load enduring, further requirements to the structure and geometry need to be defined and fulfilled. Since the aircraft will be operated in a marine environment, favourable hydrodynamic properties, such as low spray generation and minimal water resistance should be met while sea worthiness and stability need to be guaranteed.

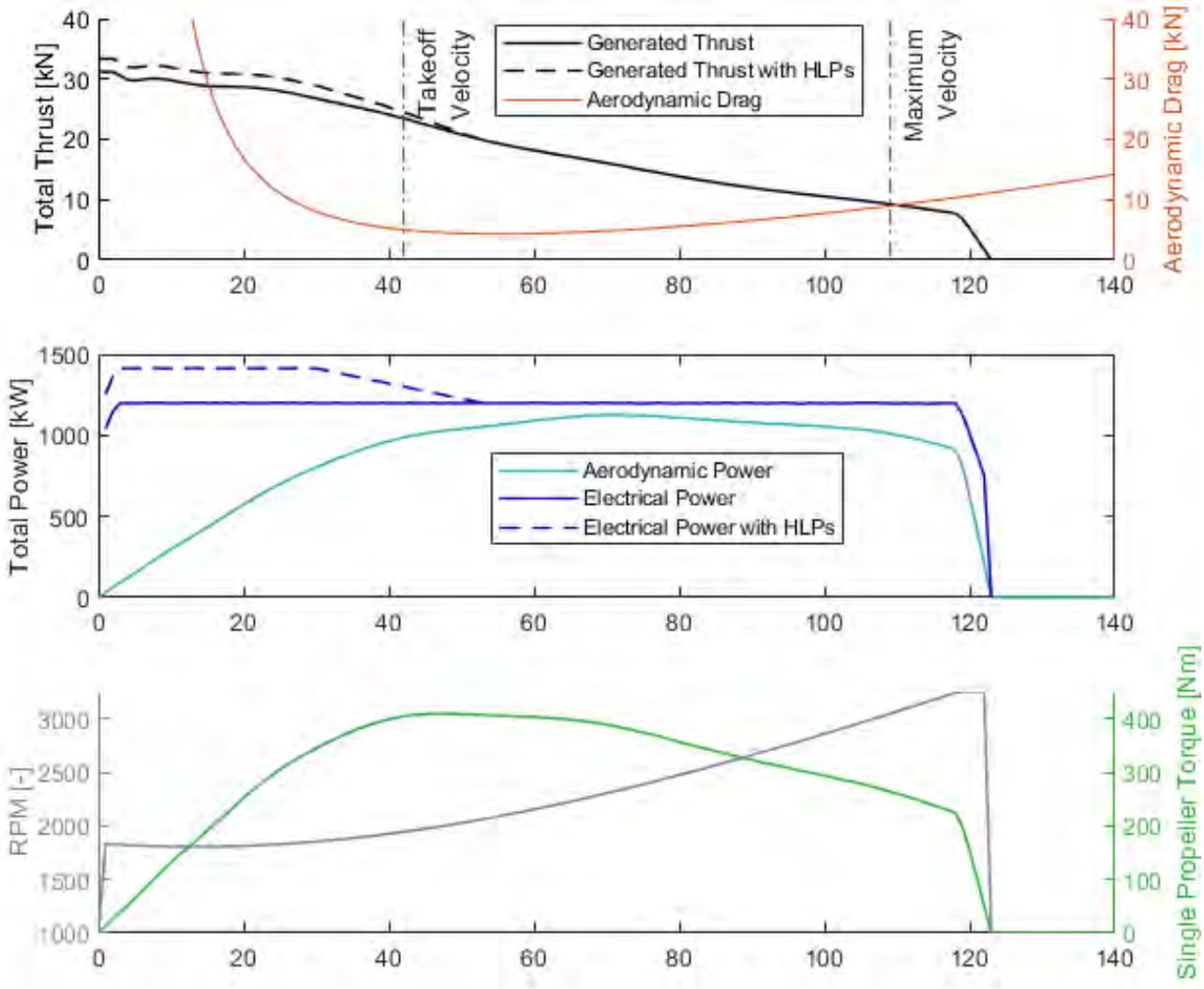

Figure 4.3: Propeller Performance

4.3.1 Naval Design

Hull and Tipfloat Geometry According to the general seaplane design process, basic geometry values such as the length of the hull and the maximum submerged width, which is called beam, need to be estimated [45]. To achieve this, the length-beam ratio L_{Hull}/B_{Hull} and the beam-loading coefficient C_a' have been examined. A hull with a length-beam ratio increasing from 6 to 12 has better aerodynamic properties (up to 20% less hull drag), and a reduced material weight (up to 8% reduced weight), since the volume is reduced [46]. Additionally, high length-beam ratios support higher beam loading up to 3, while achieving the same level of hull efficiency and seaworthiness, as less strong wave fronts and spray are developed [46]. Hull bending moments through naval operation must be kept sufficiently small. For this design prompt of a medium sized amphibious aircraft operated both in inland waters and the sea, a length-beam ratio of 9.5 and a beam loading coefficient of 2 have been chosen as design points. Figure 4.4 shows them in relation to Davidson's optimum, maximum and overload spray characteristics [47].

Using the design point values for either a constant length-beam ratio or beam loading, with respect to maximum design where $K_2 = 0.022$, a length $L_{Hull} = 13.5[m]$ and a beam $B_{Hull} = 1.42[m]$ have been calculated using the formula for the beam and respective ratios (see D.1) [45] [46].

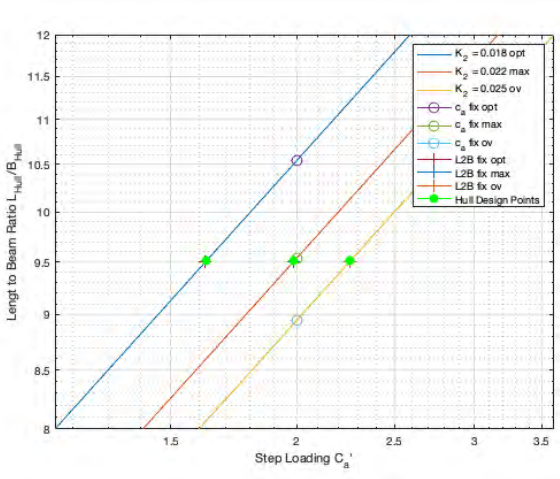

Figure 4.4: Estimation of the hull geometry based on the length-beam ratio and beam loading

With the length and the beam of the hull, further geometry as listed in table D.1 can be estimated based upon theoretical and empirical formulas provided by Gudmundsson [48] and other reference collections by Sottorf [49]. Additionally, the data was affirmed through the comparison with amphibious reference aircraft (upon [50],[51],[52],[53],[54],[55]). Similarly, the tipfloats have been estimated upon data of these reference aircraft (see D.2), while assuming advancement in the interplay with the other subsystems of the aircraft configuration until the EIS, slight reductions in sizing were considered. Such chosen data could be optimised for higher efficiency in pursuing physical tests in water tanks.

Seaplane Configuration Performance Using the stability estimation method presented by Diehl [56], *Dipper* has a longitudinal metacentric height $GM = 20.72[m]$ from the bottom of the hull. Sufficient rolling stability is provided by the tipfloats. When determining the center of buoyancy, many factors intertwine, thus most such data would result from practical experiments such as porpoising tests.

The forebody of the hull comprises 48% of the entire length with a deadrise of $20[deg]$, therefore leaving space for a prominent elongated afterbody which is inserted with the sternpost angle of $8[deg]$. A slender afterbody proves to generate less interference with the spray induced by the forebody [57]. To mitigate water spray, spray rails need to be installed on the side of the keel [46], [57]. Directional control in water is secured by a rudder connected to the vertical stabiliser. A planing tail design was chosen due to its higher takeoff and landing stability along with lower hydrodynamic resistance in comparison to conventional seaplane hulls [58]. Its particular trim to speed behaviour is modeled in graph 4.5. Using an interpolation formula from [59] (see D.4), the resistance coefficient C_R was calculated. A distinctive hump in the curve indicates the transition from volumetric displacement to planing [46]. With the corresponding speed, addressed as the hull-speed, of about $v_{Hull} = 7[m/s]$, the hull generates a wave system that induces maximum resistance. Only when the planing speed $v_{planing} = 19[m/s]$ is reached, the resistance drops to zero while water friction remains, as the hull is now gliding over the water. Having measured an approximate value for the static trim angle in the 3D-Model, the final trim angle for a planing tail craft during planing was adopted from the NACA-TN-2481 [58].

In a conservative manner, the submerged volume of the hull is estimated with submersion of the entire MTOW below water (see D.5). In accordance to the CFR §23.2310 [60] for the buoyancy of seaplanes and amphibians, which dictates a 80% excess safety margin, the hull needs to be supported by a total volume of $10.24[m^3]$. *Dipper* is equipped with several compartments filled with air and each accessible via an inspection lid. As the regulations need the design to ensure stability even after any

two compartments are flooded, the compartments are scattered and separated along the submerged part of the hull. The submerged volume decreases, when the aircraft gains more speed, as the aerodynamic lift interacts with the hydrostatic lift and the gravitational force (appendix D.5). Maintaining a conservative assumption, the hydrodynamic lift is disclosed from this calculation. Graphically measured with the static trim angle, the initially submerged area $A_{wetted,static} = 22m^2$ reduces to zero when the longitudinal forces acting on *Dipper* cancel out at a speed of about $v_{minsub} = 32[m/s]$.

Using the model for the submerged volume and wetted area in combination with the calculation of the friction after Froude [48] and the estimation of water resistance, the total water drag can be modeled in figure 4.6 and used for the takeoff estimation (see D.6).

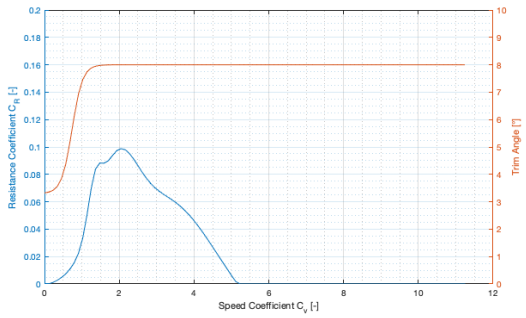

Figure 4.5: Trim angle and resistance coefficient over velocity

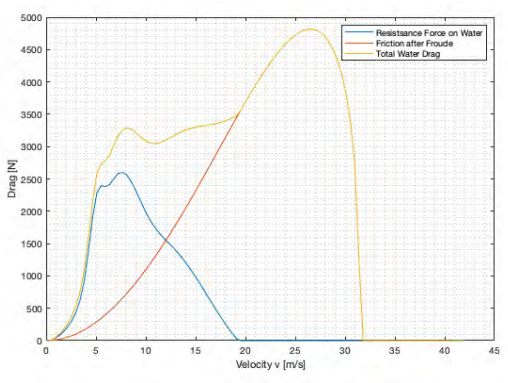

Figure 4.6: Total water drag over velocity

To further improve the takeoff and landing performance by reducing hydrodynamic drag on still bodies of water, the step needs to be ventilated. The most promising concept of a ventilation aperture directly behind a shallow and aerodynamic step (table D.3) was chosen to be fitting [61]. Potentially, retractable hydrofoils could be installed to further decrease water drag in a further design iteration [62].

4.3.2 Airframe

Due to the design as an amphibious aircraft with a boat hull, the fuselage design faces particularly specific challenges. In general, a carbon composite structure offers the most advantages for fuselage construction in aviation, such as low weight combined with high load-bearing capacity and stiffness. In addition, this material has high corrosion resistance, which is a very important influencing factor, especially when used in marine environments. However, what poses a problem is landing on the water and possible collision with flotsam. Thus, it is desirable to use a more elastic material for the bottom of the hull to avoid peak loads and to absorb the landing impacts. In addition, a collision with foreign bodies on the water could result in damage, which, especially in the case of carbon structures, can manifest itself in delamination of the individual layers and entail a costly repair process [63].

It was therefore decided to strive for a combination of carbon and aluminum structures. The upper fuselage section is to be made of carbon in order to take advantage of this material, and this in a simple cylindrical form to keep the manufacturing effort as simple and low as possible. The lower part of the hull, which represents the boat geometry, is to be made of an aluminum structure in order to meet the above-mentioned challenges with regard to elasticity and damage. However, when joining the two assemblies, great attention must be paid to the electrochemical corrosion between the two materials. Thus, care must be taken to design the targeted bonded joint in such a way that corrosion cannot take place. One possibility is to incorporate a layer of glass fiber reinforced plastic to create space between the two assemblies.

4.3.3 Landing Gear

As explained in the previous chapter, the mission design results in the amphibious design of the aircraft and thus a landing gear. The problems that arise here are the installation location and the environmental conditions. For example, when retracted, the landing gear must be above the waterline to avoid permanent contact with water, but of course, it must also be able to descend far enough to provide sufficient ground clearance when operating on the ground. In addition, lowering it in the fuselage is problematic because any indentation weakens the lightweight structure of the fuselage, but the drag of the landing gear in the retracted and extended state must also be taken into account, and accommodation in the wing box is not possible due to the necessary high-wing design. Furthermore, the omnipresent danger is the corrosive seawater, which is why complex retraction systems must be dispensed with in order to be able to execute these systems in a resistant and safe manner. As a solution to these difficulties, the following system was found.

The landing gear is designed as a typical three-point landing gear with nose wheel. In this case, the nose wheel assembly is necessarily stowed below the waterline in the hull, and special care must be taken to ensure that it is not damaged by salt water, presumably through proper sealing and a robust design.

The main landing gear is hinged at the level of the hull step. When retracted it is rotated upward toward the tail of the aircraft. It is housed in partially recessed streamlined landing gear nacelles. It is planned to continue the shape of the nacelles by means of fairings on the landing gear in order to protect the landing gear against splash water and to contribute to aerodynamics so that landing gear doors can be dispensed with.

4.4 Fire Extinguishing System

The fire extinguishing system is designed to be simple and reliable, as well as adhering to modularity for retrofit purposes.

4.4.1 Scooping Mechanism

The scooping mechanism is built into the hull step since the reinforced structure at this point provides ample opportunity for attachment points to absorb the forces acted on the mechanism by the water. It is built to be retractable to reduce drag in non-scooping flight. Figure 4.7 shows a schematic depiction of the mechanism. A linear rail is used to guide the scooping shovel which may be actuated either via a linear or circular actuator.

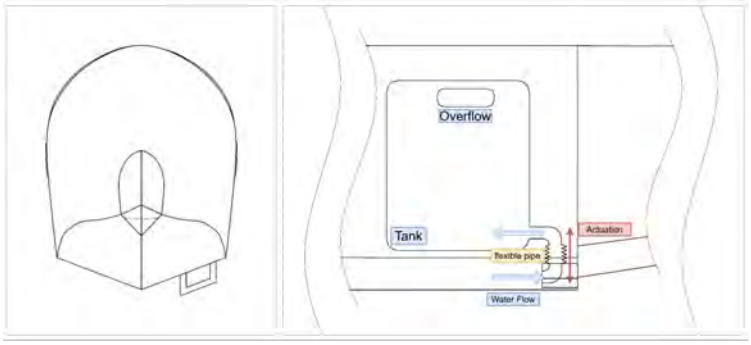

Figure 4.7: Schematic representation of the scooping mechanism

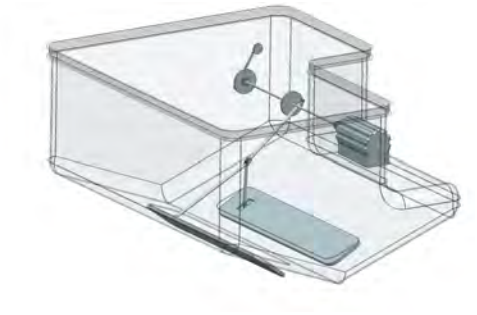

Figure 4.8: water release mechanism

4.4.2 Water Tank

For the water tank, a modular concept is employed. By splitting the tank into an upper and a lower half, upper half may be uninstalled to free up additional storage space in the aircraft fuselage. This way, the lower tank half may be used to install instrumentation that uses the line of sight from the opened flaps. Alternatively, the flaps may be closed and the lower half covered up to provide a flat inner cabin floor. The two tank halves are held together through the use of bi-stable clasps that may be positively locked through the use of a locking pin. Two sets of seals ensure no fluid escapes the tank during flight operations. A separate fire retardant tank is also connected to the upper tank half to be easily swapped out and replaced during ground operations and refueling, ensuring a fast handling time. Figures 4.9 and 4.10 contain a depiction of the tank and seals. The claps are not included in the figure.

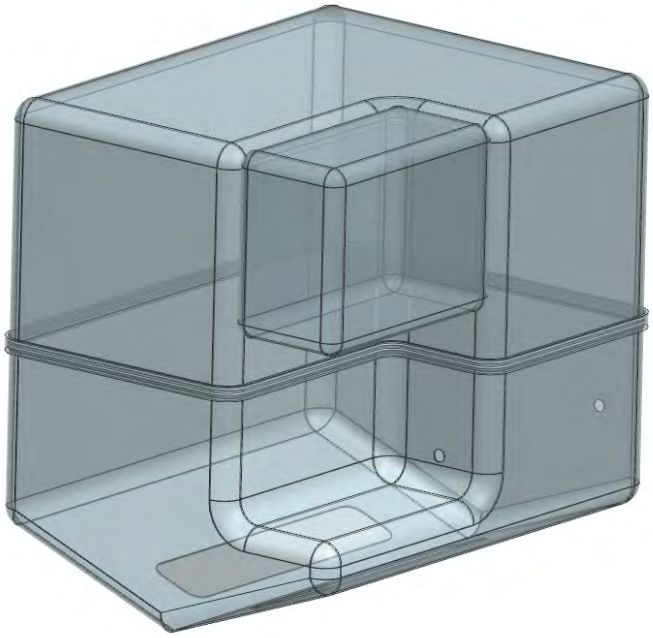

Figure 4.9: model of the water tank

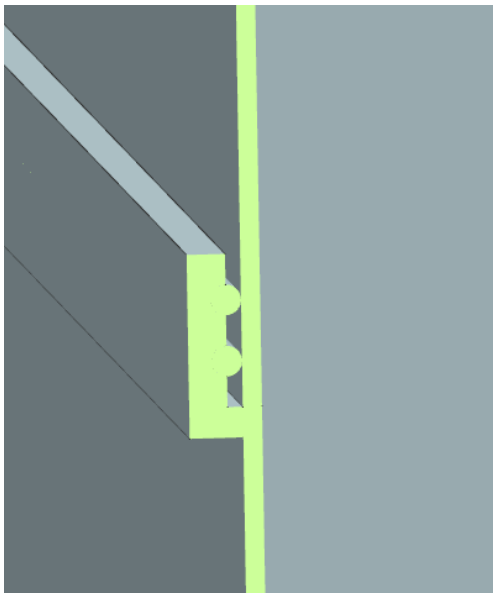

Figure 4.10: water tank seals

4.4.3 Water Release Mechanism

To release water from the tank, two flaps in the floor of the tank are used. They are connected to a servo-motor through a set of linkages. Through the use of a spring that is attached to the rod in an eccentric position, the mechanism is made bi-stable, aiding in keeping the flaps shut or open without holding the motor energized at all times. Figure 4.8 shows a model of the mechanism in a half-open position.

4.4.4 Extinguishing Chemicals

A means in forest fire fighting to the pure extinguishing water is the mixture with retardant and other extinguishing chemicals. For instance foam-chemicals can maximise drop coverage and increase ambient moisture, thereby creating an air-barrier[64]. With a mixture between 0.1 and 3 percent extinguishing agent [65], the chemical system was designed to be able to fly all firefighting attacks with water enhancer until the return to base in the standard mission. By this assumption, this

system was designed fully filled with a weight of 240 [kg]. The system should consist of a refillable extinguishing agent tank and a pump, which distribute these chemicals via a hose system to the tank sections and thus achieve sufficient mixing.

4.5 TRL Analysis

System	TRL	Criticality	Reasoning and Source
Battery	7	6	Section 4.2.7
Turbo-shaft	9	6	Section 4.2.7
Contra-rotating propellers	9	8	Section 4.2.4
Virtual pitch adjustment	1	1	Section 4.2.5
Automatic flight routing	9	9	Already in use for military purposes
high-speed satellite communication	8	9	[66]
Fleet operations	6	8	Section 6.1.2 and [67]

Table 4.4: Overview of the technology readiness level (TRL) in 2030 with the criticality for the *Dipper* and *AEGIS* design least critical (1) to most critical (9)

5 Aircraft Performance

5.1 Flight Characteristics

5.1.1 Center of Gravity and Aerodynamic Center

The Center of gravity (CG) and wing position - and by extension the aircraft aerodynamic center - are directly coupled to each other since the wing contains the fuel and therefore moving the wing has a significant influence on the CG position. Additionally, fire suppression aircraft generally undergo a sudden change in center of gravity when releasing the water stored in their tanks. Therefore, it is imperative to conduct a thorough investigation of the center of gravity behaviour of the aircraft. Since the mass is distributed mostly in symmetry to the aircraft longitudinal-horizontal plane, an investigation in this plane is sufficient. Through an iterative process, the wing position was varied along the longitudinal axis and the resulting CG configurations were investigated in their merit. Figure 5.1 shows the chosen configuration for the wing position of $x_{LE} = 4.9[m]$. This results in an aerodynamic center of $\frac{x_{AC}}{\overline{C}} = 0.534$. Table 5.1 gives an overview of the resulting center of gravity position and static margin for the edge cases. It can be seen that the most rearward CG position for the standard fire suppression mission results in $\frac{x_{CG,mr}}{\overline{C}} = 0.319$. The most forward CG position results in the case of empty weight with $\frac{x_{CG,mf}}{\overline{C}} = 0.130$. The highest CG movement in flight is in the range of $\frac{\Delta x_{CG}}{\overline{C}} \approx 0.1$ Therefore, the aircraft has a range of CG positions that accomodates the trim boundary for CG to be further back, resulting in lower control requirements for the horizontal stabilizer.

5.1.2 Lift- and Drag-Characteristics

The lift-drag polar is determined through the parabolic approximation $C_D = C_{D0} + \frac{C_L^2}{\pi e AR}$. Figure 5.2 and 5.3 show the lift and drag curves as well as the lift-to-drag ratio resulting from this. The zero-lift drag C_{D0} was determined through the method of Raymer [68] by calculating the wetted area and multiplying it with an equivalent skin friction coefficient ($C_{fe} = 0.0065$ for a prop-driven seaplane). This results in a zero-lift drag coefficient of $C_{D0} \approx 0.028$.

configuration	$\frac{x_{CG}}{C}$	static margin
with water, with fuel	0.319	0.215
w/o water, with fuel	0.218	0.102
with water, w/o fuel	0.294	0.240
w/o water, w/o fuel	0.130	0.404
average	0.240	0.294

Table 5.1: CG positions and static margins for different configurations

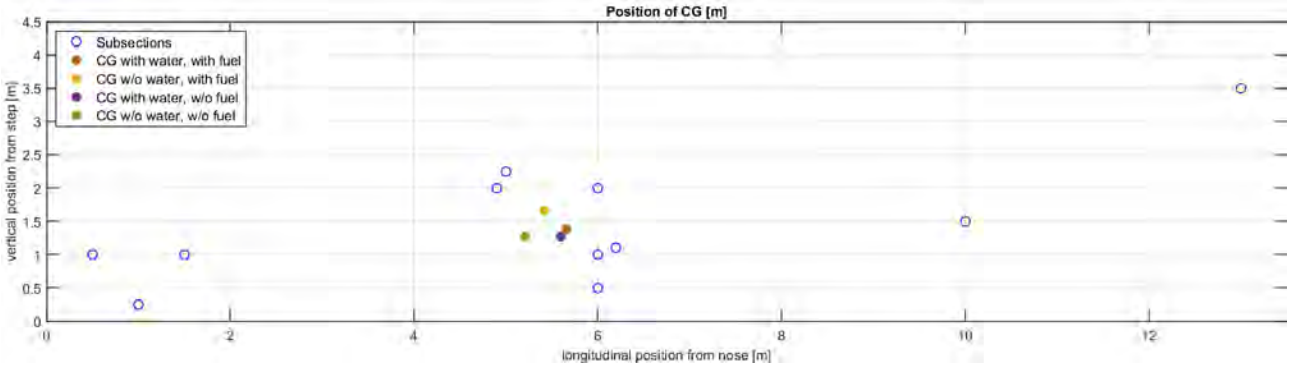

Figure 5.1: CG positions for different configurations

The Selig-3002 airfoil was ran through a two-dimensional RANS simulation for validation. The simulation was done using the mean aerodynamic chord for a Reynolds number of $Re = 1.19E7$. The resulting lift and drag coefficient in regard to the angle of attack are plotted in figure 5.4 and 5.5. This validates the goal of having a maximum lift coefficient of about $C_{L,max} \approx 2.3$ although it should be kept in mind that a finite wing has a reduced lift coefficient slope.

5.1.3 Payload-Range Diagram and Load Factor Diagram

The payload-range diagram gives an overview of the range achievable for given payload. For hybrid-electric aircraft, a range equation was developed by de Vries et al. [69]. Since in cruise flight *Dipper* uses only its turbo-shaft engine for power generation, the equation results in the traditional Breguet range equation. Using this equation, figure 5.6 plots the achievable payload for a desired range.

The load factor diagram in accordance to CS-23 [12] shows the maximum load factor at a given equivalent airspeed. As can be seen from figure 5.7, *Dipper* is designed to withstand load factors of up to $n = 4.5$, making it eligible for certification as a utility aircraft according to CS-23 [12], increasing its certified maneuver envelope. The low wing loading of the aircraft leads to susceptibility to vertical gusts, however. This is a problem that needs to be addressed before EIS. However, concepts already exist that employ active actuation of flight control surfaces to reduce gust effect [70].

5.1.4 Service Ceiling

The service ceiling is defined as the altitude at which an aircraft can just achieve a climb rate of $0.5[m/s]$. Approximating the delivered power of an air-breathing engine as an exponential curve falling from the reference power with decreasing air density and calculating the climb rate from the available power as $ROC = \frac{P_{avl}}{W}$, figure 5.8 shows the rate of climb. As can be gathered from this depiction, the rate of climb does go nearly as low as the that of the service ceiling, the altitude of which corresponds to a density of $\rho = 0.91488\ [kg/m^3]$. Therefore, the maximum start altitude for a reference turbo-shaft engine is used [71]. This gives a service ceiling of $h_{sc} = 30000\ [ft] \approx 9144\ [km]$

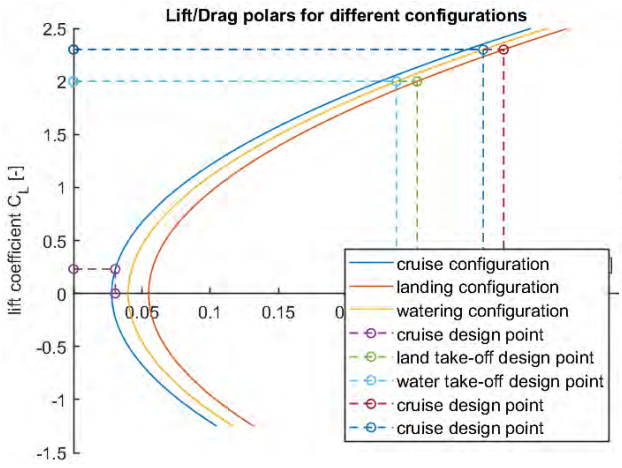

Figure 5.2: Lift-Drag Polar

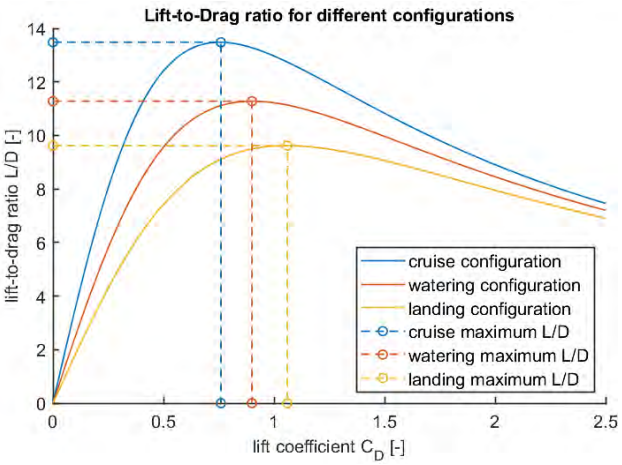

Figure 5.3: Lift-to-Drag ratio in regard to lift coefficient

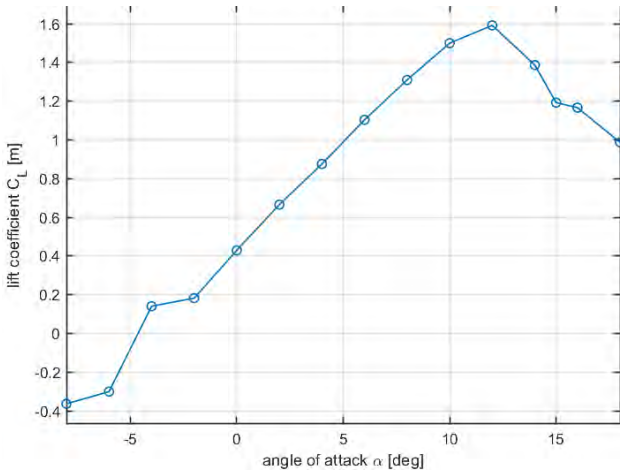

Figure 5.4: Lift coefficient in regard to angle of attack

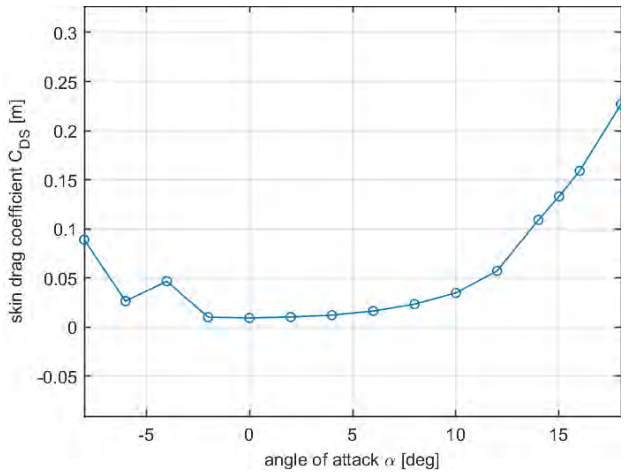

Figure 5.5: Skin drag coefficient in regard to angle of attack

on an ISA standard day. This does not include the change in pro efficiency, however. As such, the requirement of $h_{sc} > 8000[ft]$ is easily achieved, but the actual ceiling needs further investigation.

5.2 Flight Profile

For operating in a firefighting scenario, *Dipper* will start from a smaller aerodrome in the near vicinity of the fire to extinguished and picks up water from either lakes or rivers around the wildfire. Alternatively, the aircraft can also pick up salt-water from the coastline of seas. A complete mission includes starting from the base, scooping and deploying water several times and returning to base. An overview over a whole standard mission is shown in figure 5.9. Overall, in one single mission, *Dipper* will deploy approximately20 t by scooping 11 times. These values resulted from the simulations and iterative optimization processes explained in section 2. The total energy consumption for one mission is composed of the energy demand in the respective mission parts: Take-Off (T/O) from base, cruising between fire, water source and base, as well as scooping the water. A further explanation of these will be given in the following paragraphs. To calculate the energy demand for each phase, the law of momentum conservation for acceleration and deceleration and the equilibrium of forces for steady

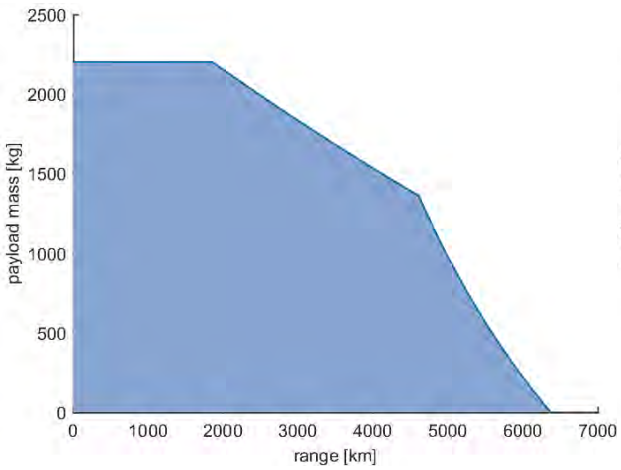

Figure 5.6: Payload-Range Diagram

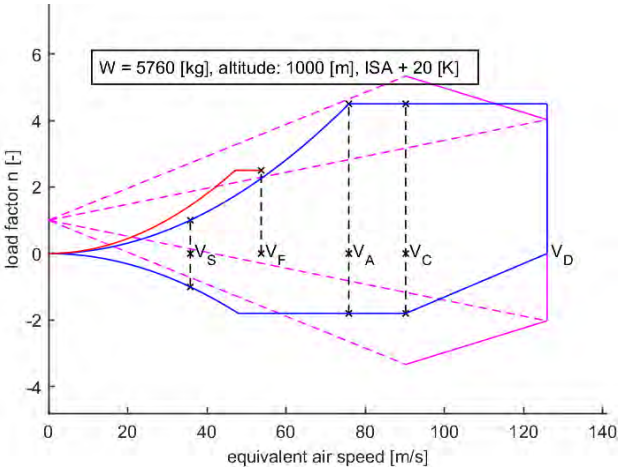

Figure 5.7: Load Factor Diagram

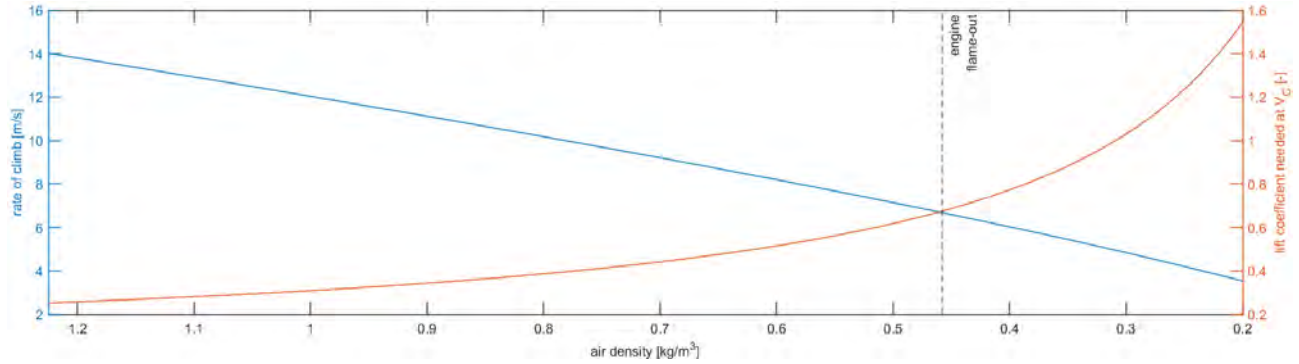

Figure 5.8: Rate of climb as a function of air density

flight states are used. Further explanations and formulas can be found in appendix E. The following table shows the overall energy demand for each mission phase of the standard benchmark mission.

	T/O @ base	cruise between operation sites	scooping	$\sum$
energy consumption $[kWh]$	5.378	2280.62	8.404	2294.4
fuel consumption $[kg]$	1.452	615.74	2.26	619.5

Table 5.2: Energy Consumption Standard Mission

Takeoff To meet the requirement of STOL capabilities, *Dipper* is able to take off from water and short paved runways and climb a minimum safe height above ground in less than 350$[m]$. This ability allows the aircraft to safely land in smaller lakes or rivers in case of an emergency or other unexpected incidents that need the plane to land, as well as enables the use as a multipurpose freighter in a second use case (section 6.3). Every take-off will follow the same procedure and consists of 3 phases:

1. An acceleration phase where the plane accelerates to rotation speed (42 [m/s])
2. The transition phase in which the aeroplane follows a circular path until the desired climb angle γ is reached and

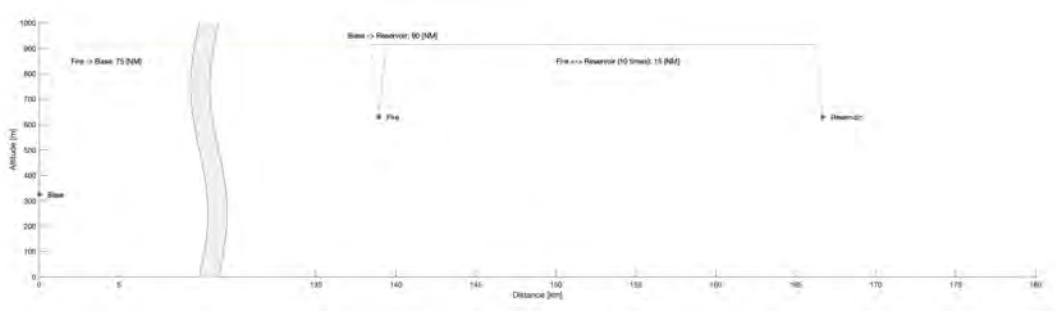

Figure 5.9: Flight Profile for the given example mission

3. An initial steady climb at constant speed (v_{rotate}) and constant path inclination γ until the minimum safe height of 20 [m] is reached.

A minimum safe height was defined as 20 [m] to keep a safe distance from objects on the ground and avoid collision with obstacles such as trees, houses or hills.

The figures E.1 and E.2 in the appendix show the flight path during a takeoff from water and from a paved runway. To estimate the most efficient climb angle γ, several simulations have been done to calculate energy consumption and T/O distance over γ. The formulas used for this purpose and the resulting diagrams can be found in Appendix E.5.

	T/O speed $[m/s]$	energy $[kWh]$	distance $[m]$	climb angle γ [deg]	climb rate $[m/s]$
T/O paved runway	42.00	5.378	227.7	28.7	20.15
T/O water ($v_{init} = 0$ $[m/s]$)	42.00	6.64	343.1	28.7	20.15
T/O water ($v_{init} = 10$ $[m/s]$)	42.00	5.85	335.3	28	19.22

Table 5.3: Performance Parameters Take-Off

To reduce the T/O distance in water, a "U-turn" can be done to get an initial speed (v_{init})before starting the T/O. With this method, the distance for this procedure can be minimized by around 10 [m].

Cruise flight between operation sites To travel between base, fire and the water reservoir, the aircraft will do a cruise flight in an altitude of 3000 [ft] MSL. To reach a minimum of energy consumed during cruise flight the cruising altitude has to be as small as possible. With a minimum ground clearance of 1000 [ft] at the fire and the water reservoir (elevation each 2000 [ft] MSL), this altitude offers a safe height on one hand and a low energy consumption on the other. Furthermore, simulations explained in section 2 showed that a cruising speed of $v = 82.00[m/s]$ between wildfire and a water reservoir, as well as $v = 90.00[m/s]$ between water reservoir and base result a maximum of water brought to the fire in a 24h interval.

This phase of the standard mission consists of the following phases:

1. steady climb at constant path inclination γ and steady $v = v_{rotate} = 42$ [m/s] until cruise altitude 3000 [ft] is reached

2. acceleration to cruise speed by using maximum available power of the engine without using the batteries

3. steady cruise at constant cruise speed alt altitude
4. descent with a steady angle γ and deceleration to v_{rotate}. During this phase, propellers are used to regain energy to fill the batteries. This recuperation is further explained in section 4.2.2.

To reach minimum energy consumption at simultaneously short time to travel between the operational bases, the path inclination for climb and descent was defined by an iterative optimization process using formulas and coherences shown in appendix E.5. Detailed results of this simulation can be found in the same paragraph.

The following table shows the overall energy consumption for a cruise flight between the 3 mission sections including climb and descent from a height of 20 [m] AGL to cruise altitude (3000 [ft]).

	speed $[m/s]$	energy $[kWh]$	climb/descent angle γ[deg]	climb rate $[m/s]$
base $\leftrightarrow$ fire	90.00	341.27	16.1	11.65
base $\leftrightarrow$ water	90.00	414.75	21.00	15.05
fire $\leftrightarrow$ water	82.00	72.60	20.00	14.37

Table 5.4: Performance Parameters Cruise

Scooping To pick up water, *Dipper* uses a method called "scooping" where the water gets pushed into the onboard water tank by the dynamic pressure caused by the plane gliding over the water surface. Figure E.3 shows the flight path of the scooping maneuver. Because the distance to scoop a defined mass of water is independent of the velocity of the scooping plane, $v_{scooping} = v_{rotate} = 42[m/s]$ was chosen for this maneuver. As with the T/O, this velocity provides a good compromise between aerodynamic and water-caused drag and offers a safe distance to stalling speed. For further explanations see Chapter 4.1. To find an optimum climb and descent angle which offers lowest energy consumption on one hand and a minimum scooping distance on the other, simulations have been done with the addition of the formulas to be found in appendix E.2 and E. The following parameters for the scooping maneuver resulted.

speed $[m/s]$	energy $[kWh]$	distance $[m]$	climb/descent angle γ [deg]	climb/descent rate $[m/s]$
42.00	0.764	209.87	18.38	13.24

Table 5.5: Performance Parameters Scooping

5.3 Noise Reduction

The propulsion and powertrain system was identified as the main source of noise. Various steps for noise abatement were proposed in section 4.2.

6 Mode of Application

6.1 AEGIS

6.1.1 System-of-System Approach

The *Aerial Extinguishing Grouped Intervention System* is a term for all aspects of the systems-of-systems approach for the showcased fire extinguishing aircraft. For one, the term describes the oper-

ative system to suppress wildfires with a multi-domain approach, including aerial and ground troops. Secondly, it describes the central software that collects live data from various sources like the European Forest Fire Information System [72] and sensors on all aircrafts to show the operators the best available data to make life-saving decisions. The system will be able to propose own solutions and strategies to counteract the fire by learning from previous missions with artificial intelligence [73]. Furthermore, *AEGIS* can optimize flight routes and cruise speeds to increase the released water amount. Simulation 2.3 shows, that an optimal cruise speed between the reservoir and fire can be found for every scenario.

A proposed operation plan is depicted in figure 6.1. A server in a High-Availability cluster collects data from various sources and contacts the aircrafts via a Low-Earth-Orbit (LEO) internet constellation as they already provide low latency and high speeds [66]. A command center in which a firefighting commander, contingency UAV pilot, air commander and a radio operator (in constant contact with Air Traffic Control) is controlling the mission. The necessary human-power can be reduced for smaller missions to reduce costs.

Figure 6.2 shows the envisioned control software in which all information are bundled to the users of *AEGIS*. With necessary peripherals an UAV pilot may take over control over the aircraft, facilitating a permit of the system until 2030.

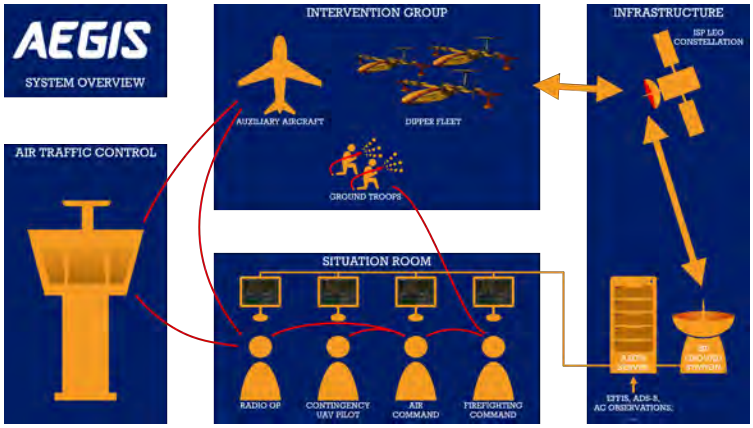

Figure 6.1: Proposed AEGIS operation structure

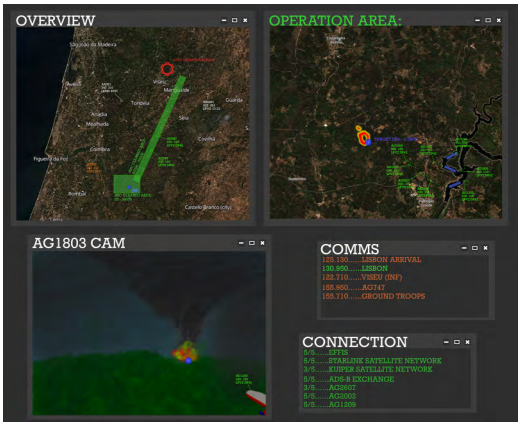

Figure 6.2: Screenshot of the proposed *AEGIS* mission control software (appendix F for higher resolution)

6.1.2 Fleet

To deliver the required attack of 11$[t]$ water, 6 or more *Dipper* aircrafts will be necessary. A totally random fleet behaviour was implemented in the simulation. That means, that every aircraft flies for itself and only waits for other aircraft at the fire to release the water. A single aircraft without hold times yields up to 150$[t]$ of water per 24 hours. With already 12 aircrafts, similar efficiencies[2] are achieved for the grouped attacks 2.4. This implies, that smart control and mission planning will improve this number and move it further to the minimum of 6 aircrafts. It is expected that 8 is a ideal fleet size for most scenarios allowing 6 aircrafts to perform extinguishing attacks and up to two aircrafts due for a refuel.

6.1.3 Remote Piloting

Dipper as part of the system-of-system concept *AEGIS* is a fully automatically controlled aircraft which communicates via control and data link connections with a mission control software and a

[2] water yield per 24 hours per aircraft

managing mission operator on the ground. To control *Dipper* in its mission scenarios, flight routes and procedures will be automatically or manually defined by the mission control software and sent to the aircraft.

The aircraft itself will take the necessary actions to follow the routes and mission procedures such as Takeoff, scooping and other. For further information about mission design and system of systems concept please see 6.1.

6.2 Operational Concept

For an operational concept stretching 24 hours, please consult section 6.1.

6.2.1 Fire Control Strategy

Wildfires behave erratic, therefore *AEGIS* must adapt rapidly to changing conditions. Valid data could be commissioned from earth observation satellite systems and local disaster detection services. With a low dropping altitude, the released water is concentrated on the spot. A direct, punctual extinguishing attack is the "Salvo" with, which can extinguish heavy canopy fires. Bushfires can be combated with a trail of water, which is more stretched than the Salvo-maneuver. Indirect attacks comprise creating such a trail of water [64]. Each water release intensity can be regulated by the aperture of the water release mechanism (section 4.4.3).

6.2.2 Coastal and Inland Mission

When operating at the coast, the physical environment needs to be accounted for. An evaluation based on the gross weight in $[lbf]$ using a conservative formula Gudmundsson [17] provides, *Dipper* will be capable of withstanding waves as high as $h_{wave} = 0.96[m]$. For instance, this makes the design adapt to intermediate wind induced wave heights in the Mediterranean Sea close to the shore [74]. To sustain higher waves on the open sea, as they occur during winter, further design measurements need to be taken. However, this maximum wave height is sufficient for fire extinguishing, as scooping would rather be conducted close to operational site.

Another challenge in the coastal scenario is the salt water, which creates conditions that strongly favor corrosion of the fuselage and assemblies. Here, navalization must be performed for all subsystems to prevent aircraft failure.

Fires from previous years within Europe were used for additional deployment scenarios, with the severe forest fires in Portugal in 2017 as a domestic scenario and the fires in Turkey in 2021 as an example selection.[3] [4]

6.2.3 Adverse Visibility

To ensure the availability of *Dipper* in preferably every weather condition as well as at day- and nighttime, the aircraft has to be fully operational also in adverse visibility. Therefore, the aeroplane has to be equipped with appropriate sensor and navigation technology. To meet this requirement, *Dipper* comes with a radar altimeter, as well as a surface scanning radar to detect obstacles or hills without the need of sunlight or in foggy conditions. Because of the comprehensive mapping in Europe, *Dipper* will (if available) use terrain maps in addition to its GPS-tracked position to get informed about its surrounding. With the help of sensor fusion of map-guided navigation and data provided by radar, thus the aircraft can be navigated securely without the need of visual sight.

6.3 Alternative Use Case

The interior of the aircraft is designed to be highly modular. Most units can be extracted or mounted from the fuselage through a cargo hatch by moving them on corresponding rails. This means only one line of production is needed, which reduces costs of infrastructure and training in manufacturing.

To make the operation of this plane as flexible as possible, *Dipper* can not only be used as an amphibious firefighting aeroplane but also to transport freight to different areas all over the world. The short takeoff and landing (STOL) capabilities enable operation also from short runways ($> 230[m]$) on regional airfields in remote areas. This qualifies the aircraft to execute transport missions e.g. in order to provide a faster[3] supply medical equipment to remote areas. Furthermore, the aircraft can be used to conduct flights with higher hazards such as scientific missions in extreme regions or over large bodies of water, as there is no crew on board at risk. To succeed, the water tank can be opened and filled with sensors (e.g. for climate observation: temperature, pollution, currents), which could also be spread through the release doors. Whenever there is a natural disaster such as a flooding, *Dipper* units or the entire fleet could be deployed swiftly on a humanitarian mission to provide relief supplies. With the short take-off and landing combined with delicate avionics and the greater *AEGIS*-System, the aircraft is highly adapt to navigating in such impassable environments.

6.4 Expense Analysis

Since *Dipper* is modular and very versatile, its cost can be mitigated. Assuming 700 flight hours per year per aircraft for the equation given from Gudmundsson [17], one unit would account for $136.000[EUR]$ in maintenance costs per year. Each engine overhaul would cost approximately $5.300[EUR]$. Landing Costs are reduced by the hybrid-electric configuration diminishing noise. Generally, given the fleet aspect, the system can be operated at justifiable costs in comparison to state-of-the-art fire extinguishing aircraft [75]: Assuming a mission duration of 3.5 hours and a fix cost per mission of the *AEGIS*-System of about $5000[EUR]$, using the formulas given in [76] the hourly operation of a *Dipper*-fleet would cost about $125000[EUR]$ with a cost per gallon of water of $0.14[EUR]$.

7 Conclusion

In this paper suitable concepts for a firefighting aircraft were examined with the prime focus on hybrid electric propulsion in combination with DEP. A service ceiling of 8000 [ft]/2438 [m] is easily exceeded, even when carrying maximum payload and fuel. It has been shown that using a conservative approach to propulsion based on available technologies, the *Dipper* aircraft concept may achieve an EIS of 2030 once few critical technologies, namely remote fleet system operation concepts and battery technology, are achieved by that time frame. Due to the hybrid-electric architechture of the platform, the powerplant may be switched out for a more sustainable option once hydrogen infrastructure becomes more thoroughly available at small airports. The aircraft may be certified in the utility category and has exceptional take-off characteristics due to its low wing loading. It has been shown that $12240[kg]$ of water can be delivered in a single approach using a fleet of six aircraft. The total amount of water delivered by a single aircraft in $24[h]$ is shown to be approximately $150[t]$. Using a modular approach the aircraft is also shown to be able to be used as a freighter outside of wildfire season with a maximum payload weight of $2200[kg]$. Regarding sustainability, *Dipper* and *AEGIS* contribute highly to the mitigation of climate impacts through their mission to effectively combat wildfires. As an outlook, the system could be further adapted to having a closed product life-cycle to reduce resource utilisation, as far as aviation safety regulations support this goal.

[3] in comparison to conventional transportation via boats

References

[1] *Commission report on forest fires: climate change is more noticeable every year*. 2021. URL: https://ec.europa.eu/commission/presscorner/detail/en/ip_21_5627 (visited on 07/11/2022).

[2] Center for Disease Control. *Aviation Safety in Wildland Firefighting*. 2016-11-29. URL: %5Curl%7Bhttps://www.cdc.gov/niosh/topics/aviation/wff.html%7D (visited on 07/11/2022).

[3] Agairupdate Staff. "Fighting Portugal's deadliest Pedrogao Grande Wildfire, the Fire Boss aspect — AgAir Update". In: *AgAir Update* (6/9/2017). URL: https://agairupdate.com/2017/09/06/fighting-portugals-deadliest-pedrogao-grande-wildfire-the-fire-boss-aspect/.

[4] Emergency Response Coordination Centre Staff. *ECHO Daily Map of 02 August 2021*. URL: https://erccportal.jrc.ec.europa.eu/ECHO-Products/Maps#/maps/3782 (visited on 07/11/2022).

[5] *CityAirbus NextGen*. 2021. URL: https://www.airbus.com/en/innovation/zero-emission/urban-air-mobility/cityairbus-nextgen (visited on 07/13/2022).

[6] *Technology Blog - Lilium*. URL: https://lilium.com/newsroom-detail/technology-behind-the-lilium-jet (visited on 07/13/2022).

[7] *X-57 Maxwell Aircraft, Nasa*. URL: https://www.aerospace-technology.com/projects/x-57-maxwell-aircraft/ (visited on 07/13/2022).

[8] Kerry G-FS Greene. *Aerial Firefighting Use and Effectiveness (AFUE) Report*. Washington, D.C., 2020. URL: https://www.fs.usda.gov/sites/default/files/2020-08/08242020_afue_final_report.pdf (visited on 07/11/2022).

[9] Horizon Magazine. *Quiet and green: Why hydrogen planes could be the future of aviation*. URL: https://ec.europa.eu/research-and-innovation/en/horizon-magazine/quiet-and-green-why-hydrogen-planes-could-be-future-aviation (visited on 07/11/2022).

[10] Aviation Magazine Staff. *Boats or Floats? - Aviation Safety*. 2002. URL: https://www.aviationsafetymagazine.com/features/boats-or-floats/ (visited on 07/11/2022).

[11] Mohammad Sadraey. *Aircraft: DesignA Systems Engineering Approach*. Chichester: Wiley, 2013. ISBN: 9781119953401.

[12] EASA. *Certification Specifications, Part 23: CS-23*.

[13] Wikipedia Community. *Category:Amphibious aircraft*. 2021-12-26. URL: https://en.wikipedia.org/wiki/Category:Amphibious_aircraft (visited on 06/13/2022).

[14] Wikipedia Community. *Aerial firefighting*. 2022-04-13. URL: https://en.wikipedia.org/wiki/Aerial_firefighting (visited on 06/13/2022).

[15] Jan Roskam. "Rapid sizing method for airplanes". In: *Journal of Aircraft* 23.7 (1986), pp. 554–560. ISSN: 0021-8669. DOI: 10.2514/3.45343.

[16] Peter Horst, Klaus Wolf, and Cord-Christian Rossow, eds. *Handbuch der Luftfahrzeugtechnik*. [Elektronische Ressource]. München: Hanser Verlag, 2014. ISBN: 9783446436046. DOI: 10.3139/9783446436046. URL: http://www.hanser-elibrary.com/doi/book/10.3139/9783446436046.

[17] Snorri Gudmundsson. *General Aviation Aircraft Design: Applied Methods and Procedures*. Elsevier Science & Technology, 2013. DOI: 10.1016/B978-0-12-397308-5.00001-5. URL: http://ebookcentral.proquest.com/lib/dhbwrv/detail.action?docID=1377690.

[18] *Manual for EMRAX Motors / Generators*. 2020. URL: https://emrax.com/wp-content/uploads/2020/03/emrax_268_technical_data_table_graphs_5.4.pdf (visited on 07/11/2022).

[19] Julian Hoelzen et al. "Conceptual Design of Operation Strategies for Hybrid Electric Aircraft". In: *Energies* 11.1 (2018), p. 217. DOI: 10.3390/en11010217.

[20] R. E. Dunham. *The potential influence of rain on airfoil performance*. Hampton, VA, 1987.

[21] H. Fatahian et al. "Numerical simulation of the efect of rain on aerodynamic performance and aeroacoustic mechanism of an airfoil via a two-phase fow approach". In: *SN Applied Sciences* 2 (2020). DOI: 10.1007/s42452-020-2685-4.

[22] Montgomery, R. C. and Moul, M T. "Analysis of deep-stall characteristics of T- tailed aircraft configurations and some recovery procedures". In: *Journal of Aircraft* 3 (1966), pp. 562–566. ISSN: 0021-8669. DOI: 10.2514/3.43777. (Visited on 07/11/2022).

[23] R. B. Walters. *Hydraulic and Electric-Hydraulic Control Systems*. Second Enlarged Edition. Springer eBook Collection. Dordrecht and s.l.: Springer Netherlands, 2000. ISBN: 978-94-015-9427-1. DOI: 10.1007/978-94-015-9427-1.

[24] Michael Selig. *UIUC Airfoil Coordinates Database*. Ed. by UIUCApplied Aerodynamics Group. Urbana-Champaign. URL: https://m-selig.ae.illinois.edu/ads/coord_database.html#S (visited on 07/11/2022).

[25] J. Bertin and R. Cummings. *Aerodynamics for Engineers*. Upper Saddle River, NJ: Pearson, 2009. ISBN: 9780132355216.

[26] R. C. Nelson. *Flight Stability and Automatic Control*. New York: McGrawHill, 1989. ISBN: 0070462186.

[27] Talal Yusaf et al. "Sustainable Aviation—Hydrogen Is the Future". In: *Sustainability* 14.1 (2022), p. 548. DOI: 10.3390/su14010548.

[28] M. Kreimeier and E. Stumpf. "Benefit evaluation of hybrid electric propulsion concepts for CS-23 aircraft". In: *CEAS Aeronautical Journal* 8.4 (2017), pp. 691–704. ISSN: 1869-5590. DOI: 10.1007/s13272-017-0269-9.

[29] Finger, Felix D., Götten, Falk, Braun, Carsten, Bil Cees, ed. *Cost Estimation Methods for Hybrid-Electric General Aviation Aircraft*. 2020. (Visited on 07/11/2022).

[30] Anna Elena Scholz, Dimitar Trifonov, and Mirko Hornung. "Environmental life cycle assessment and operating cost analysis of a conceptual battery hybrid-electric transport aircraft". In: *CEAS Aeronautical Journal* 13.1 (2022), pp. 215–235. ISSN: 1869-5590. DOI: 10.1007/s13272-021-00556-0.

[31] Darwin Jimenez et al. "Evaluation of Series and Parallel Hybrid Propulsion Systems for UAVs Implementing Distributed Propulsion Architectures". In: *Aerospace* 9.2 (2022), p. 63. DOI: 10.3390/aerospace9020063.

[32] Alex M. Stoll et al. "Drag Reduction Through Distributed Electric Propulsion". In: *14th AIAA Aviation Technology, Integration, and Operations Conference*. Reston, Virginia: American Institute of Aeronautics and Astronautics, 2014. ISBN: 978-1-62410-282-0. DOI: 10.2514/6.2014-2851.

[33] Egbert Torenbeek. *Advanced aircraft design: Conceptual design, analysis, and optimization of subsonic civil airplanes*. Aerospace series. Chichester: Wiley, 2013. ISBN: 978-1-118-56811-8.

[34] David Erzen, Matej Andrejasic, and Tadej Kosel. "An Optimal Propeller Design for In-Flight Power Recuperation on an Electric Aircraft". In: *2018 Aviation Technology, Integration, and Operations Conference*. Reston, Virginia: American Institute of Aeronautics and Astronautics, 2018. ISBN: 978-1-62410-556-2. DOI: 10.2514/6.2018-3206.

[35] Nicholas K. Borer and Michael D. Patterson. "X-57 High-Lift Propeller Control Schedule Development". In: *NASA Langley Research Center, Hampton, Virginia, 23681, USA*. URL: https://ntrs.nasa.gov/api/citations/20205010303/downloads/Borer_Patterson_high-lift_propeller_schedule-manuscript-final_2020-05-05.pdf (visited on 07/11/2022).

[36] J. S. Vanderover and K. D. Visser. "Analysis of a Contra-Rotating Propeller Driven Transport Aircraft". In: *Clarkson University, Potsdam, New York, 13699-5725* (2000).

[37] David Biermann and W. H. Gray. *WIND-TUlNNEL TESTS OF SINGLE- AND DUAL-ROTATING PUSHER PROPELLERS HAVING FROM THREE TO EIGHT BLADES*. 1942.

[38] Maria Grazia de Giorgi et al. "Numerical investigation of the performance of Contra-Rotating Propellers for a Remotely Piloted Aerial Vehicle". In: *Energy Procedia* 126 (2017), pp. 1011–1018. ISSN: 18766102. DOI: 10.1016/j.egypro.2017.08.273.

[39] Fritz Dubs. *Aerodynamik der reinen Unterschallströmung*. 6. Aufl., (unveränd. Nachdr. d. 4. Aufl.) Vol. 1. Flugtechnische Reihe. Basel, Boston, and Stuttgart: Birkhäuser, 1990. ISBN: 3764318724.

[40] Yasa. *YASA 750R E-Motor*. 2019. URL: https://www.yasa.com/wp-content/uploads/2021/05/YASA-750RDatasheet-Rev-11.pdf (visited on 07/11/2022).

[41] EASA. *TYPE-CERTIFICATE for ARRANO 1 engine series*. 2020.

[42] Grietus Mulder et al. "Comparison of commercial battery cells in relation to material properties". In: *Electrochimica Acta* 87 (2013), pp. 473–488. ISSN: 00134686. DOI: 10.1016/j.electacta.2012.09.042.

[43] Tobias Placke et al. "Lithium ion, lithium metal, and alternative rechargeable battery technologies: the odyssey for high energy density". In: *Journal of Solid State Electrochemistry* 21.7 (2017), pp. 1939–1964. ISSN: 1432-8488. DOI: 10.1007/s10008-017-3610-7.

[44] Mohd Tariq et al. "Aircraft batteries: current trend towards more electric aircraft". In: *IET Electrical Systems in Transportation* 7.2 (2017), pp. 93–103. ISSN: 2042-9738. DOI: 10.1049/iet-est.2016.0019.

[45] Elmar Wilczek. *Seaplane Design - A Forgotten Art*. Hamburg, 2021. DOI: 10.5281/ZENODO.4781082. URL: https://www.fzt.haw-hamburg.de/pers/Scholz/dglr/hh/text_2021_05_20_SeaplaneDesign.pdf.

[46] Ernest G. Stout. "Development of High-Speed Water-Based Aircraft". In: *Journal of the aeronautical Sciences* 17 (1950), pp. 457–480. URL: https://repository.tudelft.nl/islandora/object/uuid:89dd09ca-c5d8-461d-96dd-d1e879cd570a/datastream/OBJ/download.

[47] National Advisory Committee for Aeronautics (NACA), ed. *General Tank Tests on the hydrodynamic Characteristics of four Flying-Boat Hull Models of differing length-beam Ratio*. 1944. URL: https://apps.dtic.mil/sti/pdfs/ADB804995.pdf.

[48] Snorri Gudmundsson. *General Aviation Aircraft Design: Applied Methods and Procedures: Appendix C3*. 2013.

[49] W. Sottorf. *The Design of Floats*. Ed. by National Advisory Committee for Aeronautics (NACA). 1938. URL: https://ntrs.nasa.gov/api/citations/19930094556/downloads/19930094556.pdf.

[50] *Viking Aircraft Firefighting: Specifications*. URL: https://aerialfirefighter.vikingair.com/firefighting/specifications (visited on 07/11/2022).

[51] Beriev Aircraft Company. *Be-200: Multipurpose Amphibious Aircraft*. URL: https://www.beriev.com/eng/Be-200_e/Be-200_e.html (visited on 07/10/2022).

[52] Mark Finlay. 2022. URL: https://simpleflying.com/the-shinmaywa-us-2-japans-stol-seaplane/ (visited on 07/10/2022).

[53] *Martin P6M Sea Master*. URL: http://www.aviastar.org/air/usa/martin_seamaster.phpMartin%20P6M%20Sea%20Master (visited on 07/10/2022).

[54] *Martin PBM Mariner: Patrol bomber flying boat introduced in 1940*. URL: https://aerocorner.com/aircraft/martin-pbm-mariner/ (visited on 07/10/2022).

[55] K Palt. *Grumman G-64 (HU-16/SA-16) / G-111 Albatross: Mehrzweck Ambhibienflugzeug*. URL: http://www.flugzeuginfo.net/acdata_php/acdata_g64_dt.php (visited on 07/10/2022).

[56] W. S. Diehl and W. C. Axt. *Static Stability of Seaplane Floats and Hulls*. Ed. by National Advisory Committee for Aeronautics (NACA). 1924. URL: https://www.abbottaerospace.com/downloads/naca-tn-183-static-stability-of-seaplane-floats-and-hulls/?wpdmdl=2918&ind=1461085672585.

[57] W. C. Jr. Hugli. *Hydrodynamic Investigation of a Series of Hull Models Suitable for Small Flying Boats and Amphibians*. Ed. by National Advisory Committee for Aeronautics (NACA). 1951.

[58] Henry B. Suydam. *Hydrodynamic Characteristics of a Low Drag Planing Tail Flying Boat Hull*. Ed. by National Advisory Committee for Aeronautics (NACA). Washington, 1952. URL: https://www.abbottaerospace.com/downloads/naca-tn-2481-hydrodynamic-characteristics-of-a-low-drag-planing-tail-flying-boat-hull/?wpdmdl=28992&ind=1483987222815.

[59] S. Chinvorarat. *Take-off Performance Analysis of a Light Amphibious Airplane*. Ed. by IOP Conference. 2021. DOI: 10.1088/1757-899X/1137/1/012010. URL: https://iopscience.iop.org/article/10.1088/1757-899X/1137/1/012010/pdf.

[60] *Code of Federal Regulations: § 23.2310 Buoyancy for seaplanes and amphibians*. URL: https://www.ecfr.gov/current/title-14/chapter-I/subchapter-C/part-23/subpart-D/section-23.2310 (visited on 06/24/2022).

[61] James M. Benson and Robert F. Havens. *Tank Tests of a Flyig-Boat Model equipped with several Types of Fairing dsigned to reduce the Air Drag of the main Step*. Ed. by National Advisory Committee for Aeronautics (NACA). Washington, 1945. URL: https://ntrs.nasa.gov/api/citations/19930093023/downloads/19930093023.pdf.

[62] Arjit Seth and Rhea P. Liem. "Amphibious Aircraft Developments: Computational Studies of Hydrofoil Design for Improvements in Water-Takeoffs". In: *Aerospace* 8.1 (2021), p. 10. DOI: 10.3390/aerospace8010010.

[63] M.S Sohn et al. "Impact damage characterisation of carbon fibre/epoxy composites with multi-layer reinforcement". In: *Composites Part B: Engineering* 31.8 (2000), pp. 681–691. ISSN: 1359-8368. DOI: 10.1016/S1359-8368(00)00028-7. URL: https://www.sciencedirect.com/science/article/pii/S1359836800000287.

[64] *CL415 irefighting technique*. URL: https://aerialfirefighter.vikingair.com/firefighting/firefighting-technique (visited on 05/20/2022).

[65] C. Bullock. *Aerial firefighting: How effective are water enhancers?* 2020. URL: https://www.airmedandrescue.com/latest/long-read/aerial-firefighting-how-effective-are-water-enhancers (visited on 07/09/2022).

[66] Joey Roulette. *SpaceX's Starlink is in talks with 'several' airlines for in-flight Wi-Fi*. 2021-07-09. URL: https://www.theverge.com/2021/6/9/22526601/elon-musk-spacex-starlink-internet-talks-commercial-airlines-in-flight-wifi (visited on 07/08/2022).

[67] Dominic Vogel and Stiftung Wissenschaft und Politik. *Future Combat Air System: too big to fail*. 2021. DOI: 10.18449/2021C02.

[68] D. P. Raymer. *Aircraft Design: A Conceptual Approach*. Transatlantic Publishers, 2012. ISBN: 978-1-62410-490-9.

[69] De Vries et al. *Range Equation for Hybrid-Electric Aircraft with Constant Power Split*. 2020. DOI: 10.2514/1.C035734.

[70] R. Kelm and M. Grabietz. "Method for reducing gust loads on an aircraft below the cruising altitude". DE19819341A1. 1999. URL: https://patents.google.com/patent/DE19819341A1/en.

[71] Honeywell International Inc., ed. *TPE331-10 Turboprop Engine*. Phoenix, AZ, 2016. URL: https://aerospace.honeywell.com/us/en/products-and-services/product/hardware-and-systems/engines/tpe331-turboprop-engine (visited on 07/11/2022).

[72] EFFIS Staff. *European Forest Fire Information System*. URL: https://effis.jrc.ec.europa.eu (visited on 07/10/2022).

[73] World Economic Forum Staff. *How AI can help the world fight wildfires*. 2022-05-18. URL: https://www.weforum.org/agenda/2022/05/how-ai-can-help-the-world-fight-wildfires/ (visited on 07/07/2022).

[74] F. Barbariol and S. Davison. *Wind Waves in the Mediterranean Sea: An ERA5 Reanalysis Wind-Based Climatology*. 2021. DOI: 10.3389/fmars.2021.760614. URL: https://www.frontiersin.org/articles/10.3389/fmars.2021.760614/full.

[75] FIRE BOSS - Aerial Firefighting Solution. *The most economical Solution*. 2022. URL: https://firebossllc.com/cost-comparison/ (visited on 08/02/2022).

[76] P. S. Prakasha et al. *Exploration of aerial Firefighting Fleet Effectiveness and Cost by Systems of Systems Simulations*. 2021. URL: https://elib.dlr.de/148125/1/Exploration%5C%20of%5C%20Aerial%5C%20Firefighting%5C%20Fleet%5C%20Effectiveness%5C%20and%5C%20Cost%5C%20by%5C%20System%5C%20of%5C%20Systems%5C%20Simulations_ICAS2020_0997_paper.pdf (visited on 08/02/2022).

A Initial Sizing

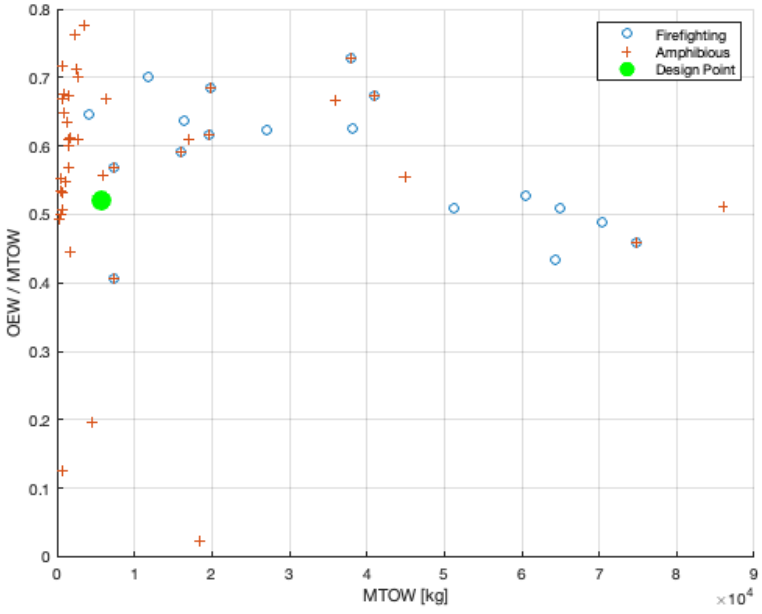

Figure A.1: Initial Mass Estimation

B Propulsion

B.1 Diagrams

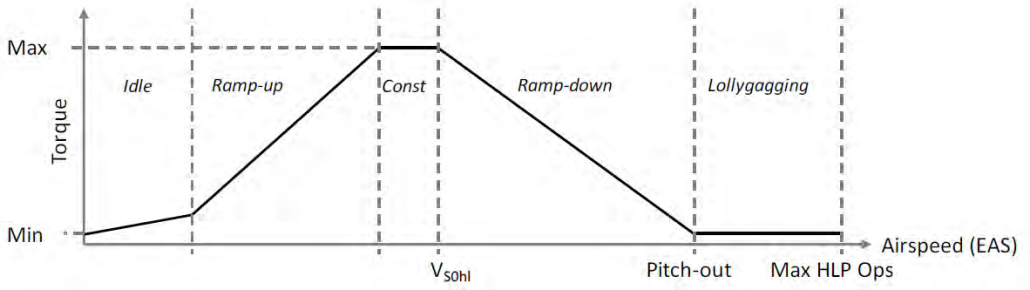

Figure B.1: HLP Torque curve [35]

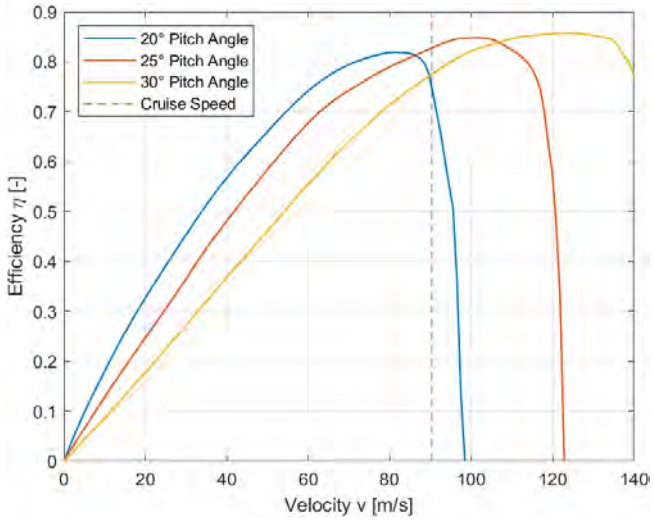

Figure B.2: Efficiency over velocity for maximum design RPM

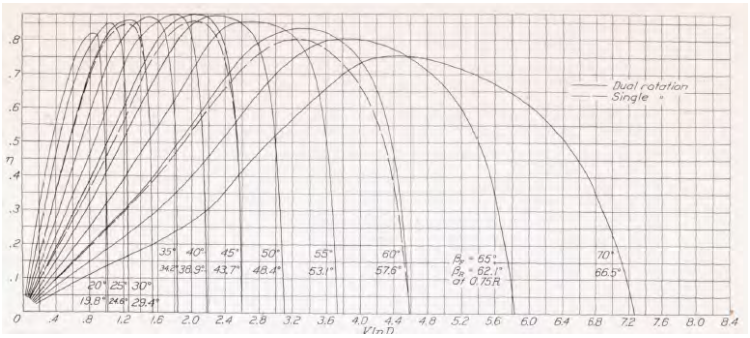

Figure B.3: Efficiency over advance ratio $J = \frac{v}{n \cdot D}$

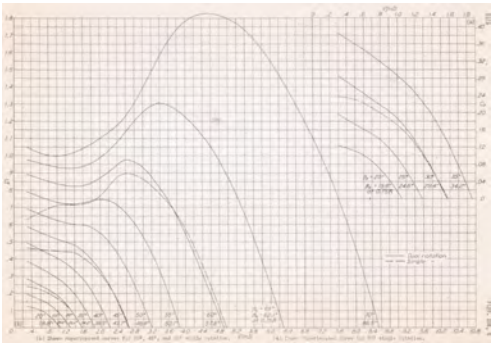

Figure B.4: Power coefficient 4 over advance ratio $J = \frac{v}{n \cdot D}$

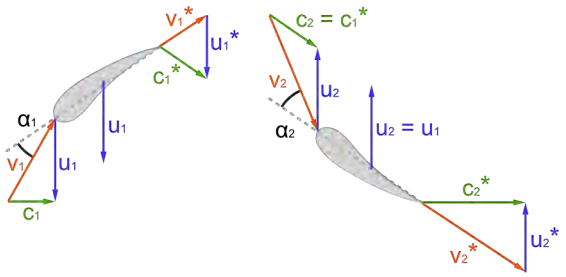

Figure B.5: Velocity vectors with equal RPM for front- and rear propeller

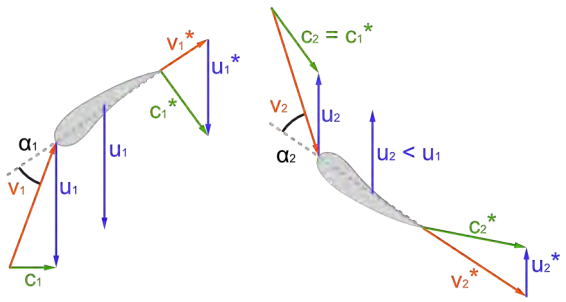

Figure B.6: Velocity vectors with different RPM for front- and rear propeller

B.2 Propeller Calculations

The ideal power is calculated by the following equation [48]:

$$P = T \cdot v \cdot \tag{2}$$

The real power is calculated by the following equation [48]:

$$P = \frac{T \cdot v}{\eta} \tag{3}$$

The power coefficient according to [37] is described as:

$$c_P = \frac{P}{\rho \cdot n^3 \cdot \cdot D^5} \tag{4}$$

The maximum diameter is determined using:

$$D = \frac{\sqrt{v_{\infty_{max}} + Ma_{max} \cdot \kappa \cdot R \cdot T}}{\pi \cdot n} \tag{5}$$

Derived with following formula [48]:

$$Ma = \sqrt{\kappa \cdot R \cdot T} \qquad v^2_{tip_{max}} = v^2_{\infty_{max}} + (\pi \cdot n \cdot D)^2 \tag{6}$$

C Aerodynamics

Horizontal Stabilizer			Vertical Stabilizer		
hor. span b_h	7.84	$[m]$	vert. span b_v	2.65	$[m]$
hor. root chord $C_{r,h}$	1.84	$[m]$	vert. root chord $C_{r,v}$	2.25	$[m]$
hor. tip chord $C_{t,h}$	1.10	$[m]$	vert. tip chord $C_{t,v}$	1.84	$[m]$
hor. angle of incidence i_h	-3.8	$[deg]$	vert. angle of incidence i_v	0	$[deg]$
hor. twist angle $\alpha_{t,h}$	0	$[deg]$	vert. twist angle $\alpha_{t,v}$	0	$[deg]$
hor. leading edge sweep $\varphi_{LE,h}$	0	$[deg]$	vert. leading edge sweep $\varphi_{LE,v}$	8.8	$[deg]$
hor. planform area S_h	11.52	$[m^2]$	vert. planform area S_v	5.42	$[m^2]$
hor. aspect ratio AR_h	5.32	$[-]$	vert. aspect ratio AR_v	1.30	$[-]$
hor. MAC $\overline{C}_h$	1.50	$[m]$	vert. MAC $\overline{C}_v$	2.05	$[m]$
hor. taper ratio λ_h	0.60	$[-]$	vert. taper ratio λ_v	0.82	$[-]$
hor. stab. volume coefficient V_h	0.70	$[-]$	vert. stab. volume coefficient V_v	0.039	$[-]$

Table C.1: Stabilizer geometry

D Naval Design

D.1 Beam Calculation

$$B_{Hull} = \sqrt[3]{\frac{MTOW}{\rho_w \cdot C_a'}} \tag{7}$$

D.2 Reference Amphibious Aircraft

Estimating the tipfloat design points based on existing amphibious aircraft.

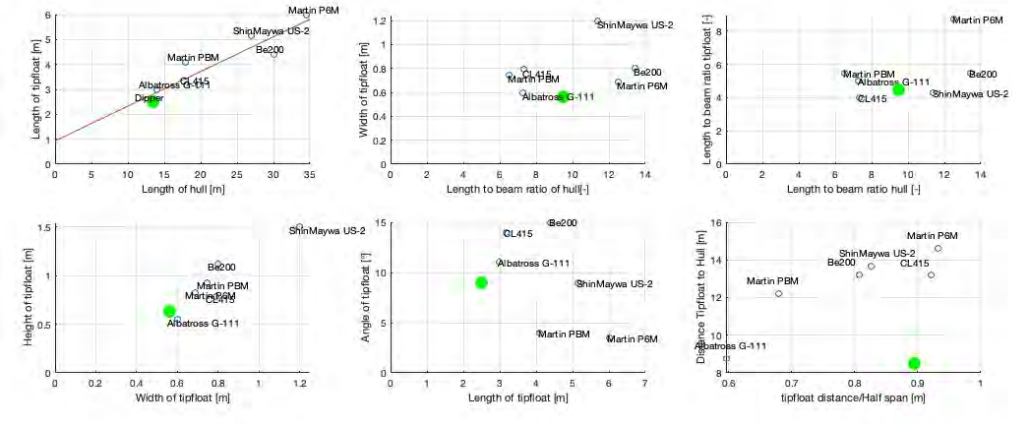

Figure D.1: Dipper in Comparison to different reference Amphibious Aircraft

D.3 Hull and Tipfloat geometry

Table D.1: Hull Geometry Values after [47],[56],[48]

Subject	Geometry	Value	Unit
Hull	Length of Hull	13.5	[m]
	Beam of Hull	1.42	[m]
	Submerged Hull Volume	5.687	[m]
	Length of forebody	6.5	[m]
	Length of afterbody	7	[m]
	Height of Step	0.09	[m]
	Step Ventilation	0.14	$[m^2]$
	Deadrise Angle	20	[°]
	Sternpost Angle	8	[°]
	Static Trim Angle	3.3	[°]
	Trim Angle at Take-off	8	[°]
Tipfloats	Water-Angle to Tipfloats	3	[°]
	Length of Tipfloat	2.5	[m]
	Beam of Tipfloat	0.56	[m]
	Height of Tipfloat	0.63	[m]
	Angle of Installation	9	[°]
	Distance on Halfspan	8.5	[m]

D.4 Interpolation Formula for the resistance coefficient

The interpolation formula is taken from [59] which bases itself upon [58].

$$C_R = 0.05789 \cdot e^{(-(\frac{C_v - 1.907}{0.7561})^2)} + 0.0273 \cdot e^{(-(\frac{C_v - 1.347}{0.2536})^2)} - 0.3322 \cdot e^{(-(\frac{C_v - 23.41}{11.74})^2)} + 0.07924 \cdot e^{(-(\frac{C_v - 3.227}{1.951})^2)} \tag{8}$$

D.5 Submerged Volume and Wetted Area

$$V_{sub}(v) = \frac{MTOW}{\rho_w} - c_{L,max} \cdot 0.5 \cdot \rho(h)_{ISA} \cdot v^2 \frac{S}{g \cdot \rho_w} \tag{9}$$

The formula for the wetted area was modeleded assuming a simple prism geometry for the hull with average values for deadrise, and wetted length.

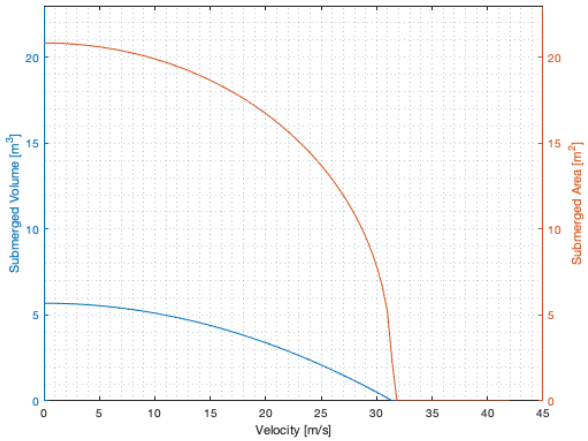

Figure D.2: Submerged Volume and Wetted Area over velocity

D.6 Friction after Froude

The friction after froude is calculated in imperial units (ft^2, kts and solution then converted to metric units).

$$R_{Froude} = f \cdot A_{wetted} \cdot v^2 \tag{10}$$

E Flight Profile

E.1 Calculation Power Consumption

The estimation of the needed power for each phase in a mission was done be by using the following formula for steady cruise, climb or descent:

$$F_{thrust} = \left[c_{w0} + \frac{1}{\pi \cdot e \cdot \Lambda} \cdot \left(\frac{MTOW \cdot g \cdot sin(\gamma)}{\frac{v^2}{2} \cdot \rho \cdot S} \right)^2 \right] \cdot \frac{v^2}{2} \cdot \rho \cdot S + MTOW \cdot g \cdot sin(\gamma) \tag{11}$$

For accelerated or decelerated movements while accelerating from standstill to rotation speed and from rotation speed to cruise speed:

$$F_{thrust} = MTOW \cdot a + \left[c_{w0} + \frac{1}{\pi \cdot e \cdot \Lambda} \cdot \left(\frac{MTOW \cdot g \cdot sin(\gamma)}{\frac{v^2}{2} \cdot \rho \cdot S} \right)^2 \right] \cdot \frac{v^2}{2} \cdot \rho \cdot S + W_{water} \tag{12}$$

For calculating the resulting power and energy:

$$P = F_{thrust} \cdot v_{rotate} \tag{13}$$

$$E = P \cdot t \tag{14}$$

E.2 Distance Calculation

To estimate the distance and time traveled during each phase of the mission, the following equation were used. For steady cruise, climb and descent:

$$s = v \cdot t \tag{15}$$

For accelerated or decelerated movements while accelerating from standstill to rotation speed and from rotation speed to cruise speed:

$$t = t_0 + \frac{v_1 - v_2}{a} \tag{16}$$

$$s = \frac{v_1^2 - v_2^2}{2 \cdot a} \tag{17}$$

E.3 Takeoff Paths

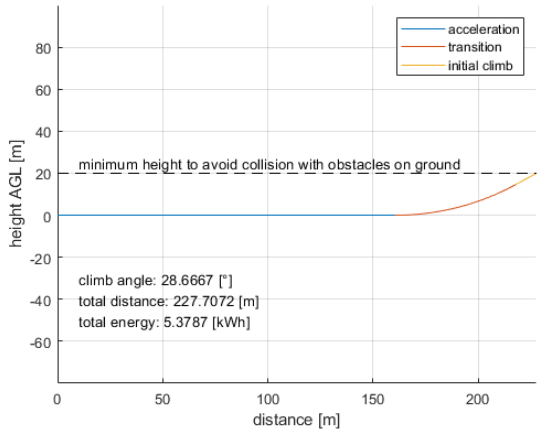

Figure E.1: T/O path from dry runway

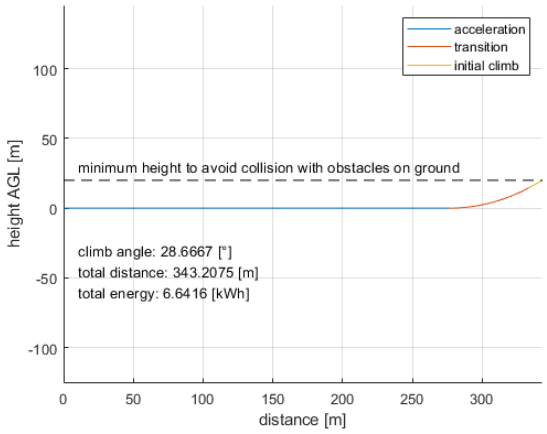

Figure E.2: T/O path from water

E.4 Scooping Profile

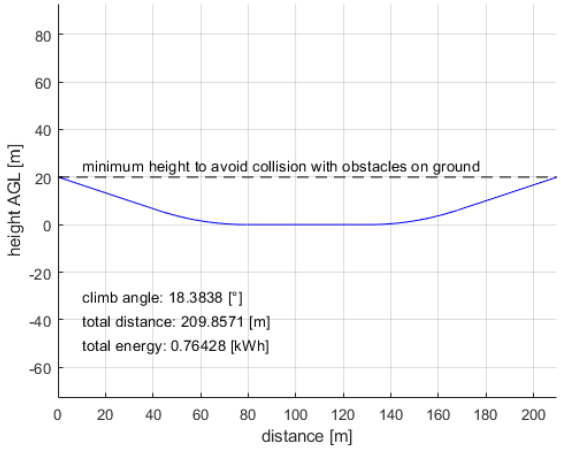

Figure E.3: Profile scooping

E.5 Optimization of climb and descent angle

Takeoff

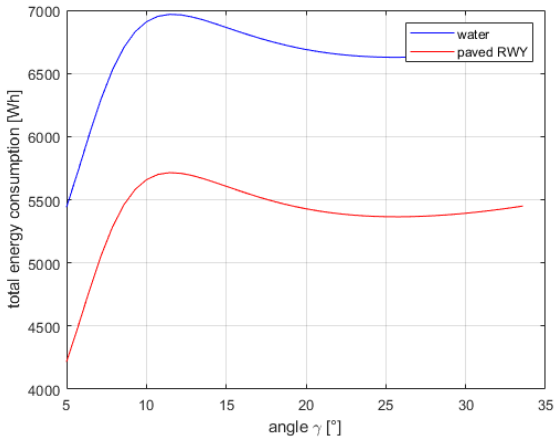

Figure E.4: T/O energy consumption over γ

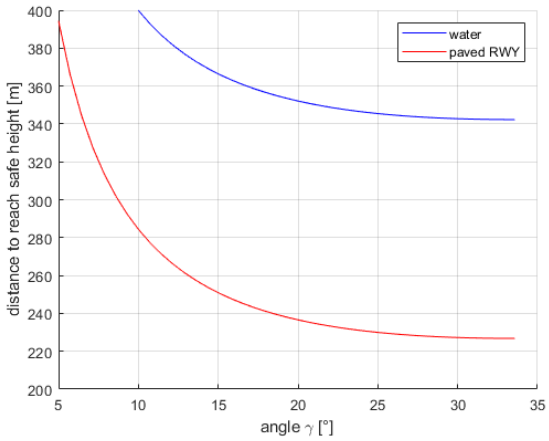

Figure E.5: T/O distance over γ

Climb - Cruise - Descent between base and reservoir

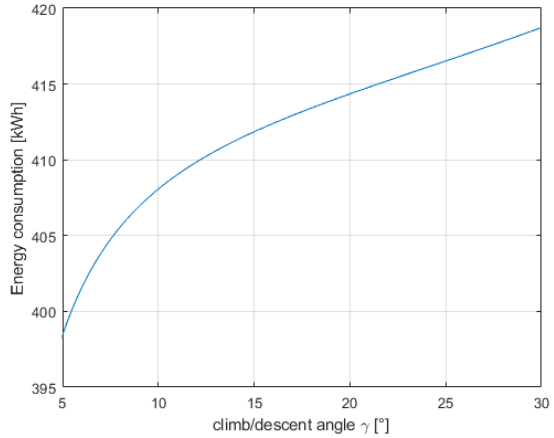

Figure E.6: base ↔ water reservoir energy consumption over γ

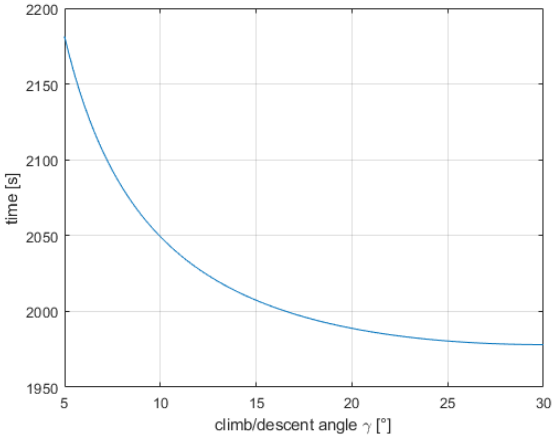

Figure E.7: base ↔ water reservoir time to travel over γ

Climb - Cruise - Descent between base and fire

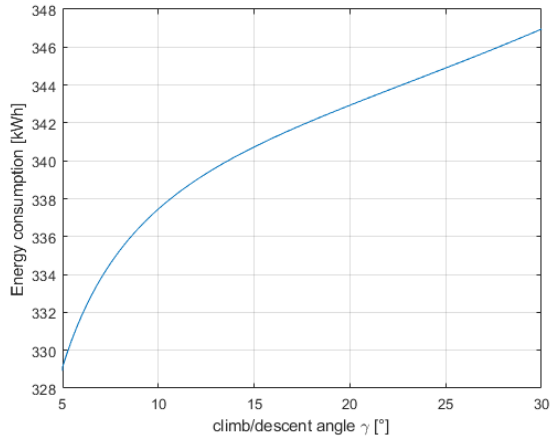

Figure E.8: base ↔ fire energy consumption over γ

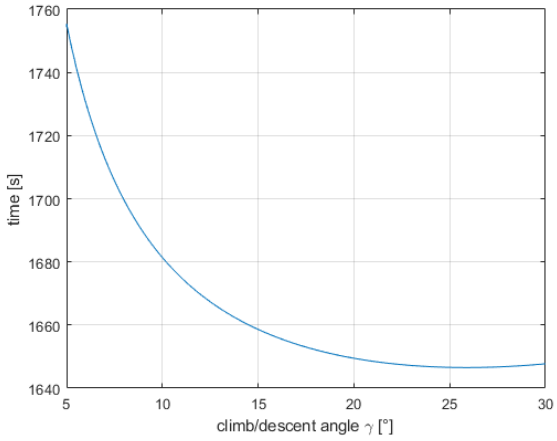

Figure E.9: base ↔ fire time to travel over γ

Climb - Cruise - Descent between reservoir and fire

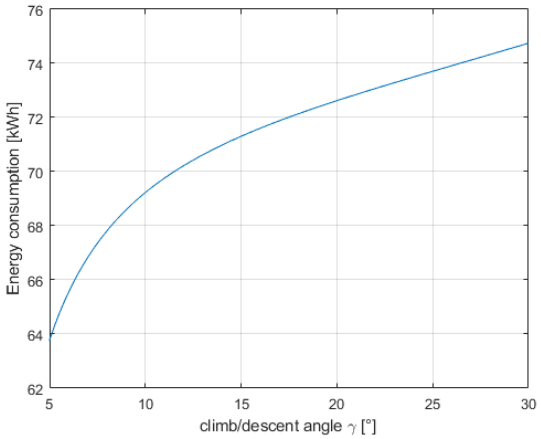

Figure E.10: water reservoir ↔ fire energy consumption over γ

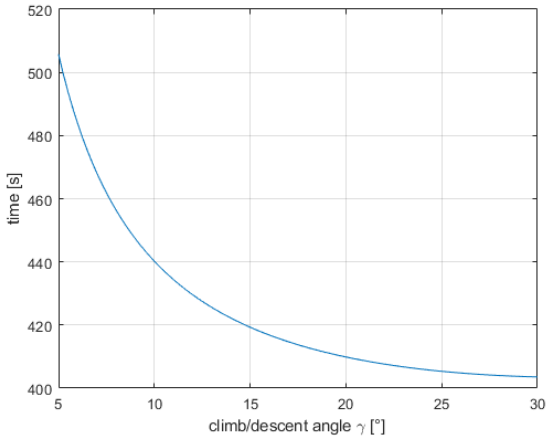

Figure E.11: water reservoir ↔ fire time to travel over γ

F Mode of Application

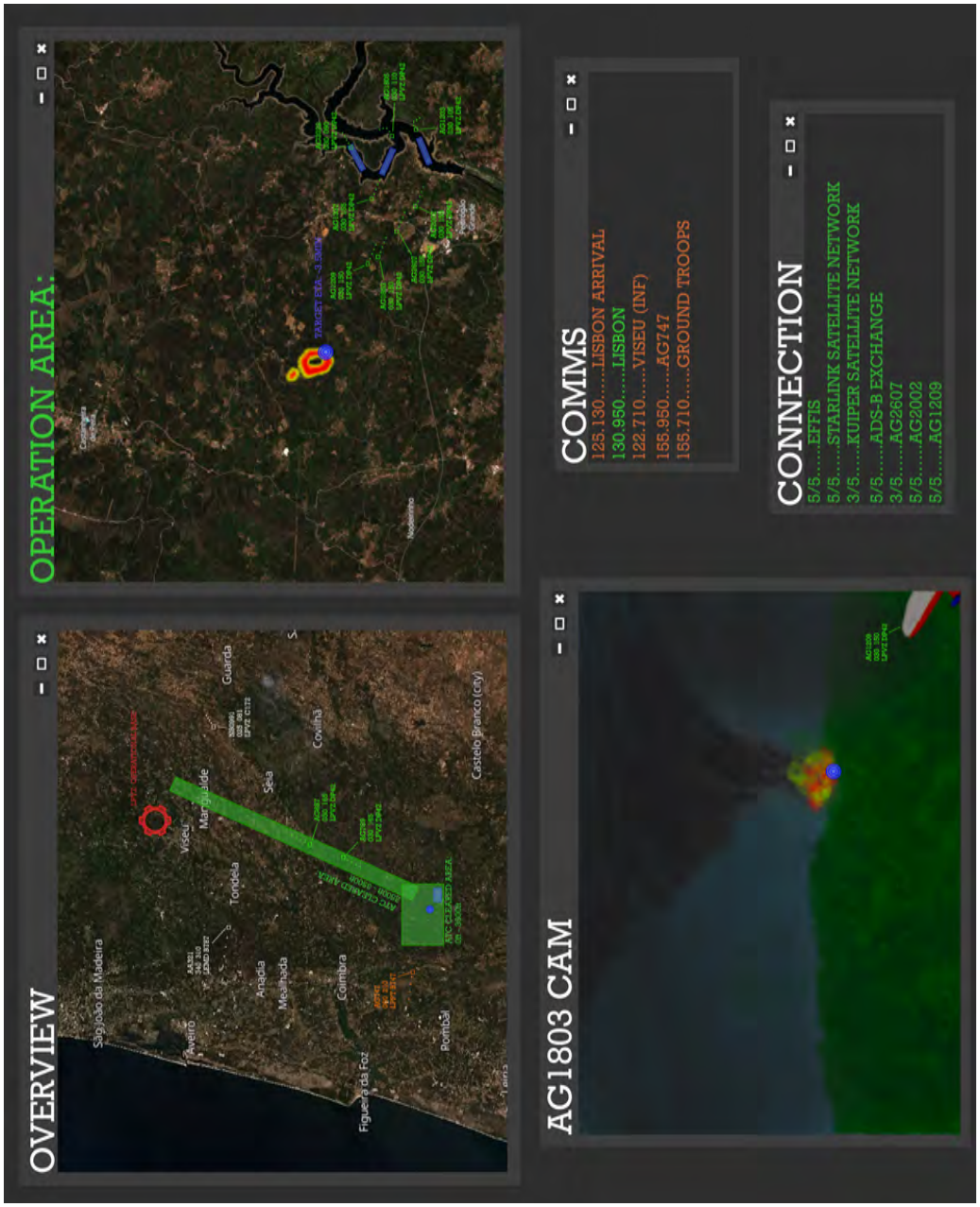

Figure F.1: Screenshot of the proposed *AEGIS* mission control software